(Preprint) AAS 11-535

RADAR ALTIMETRY AND VELOCIMETRY FOR INERTIAL NAVIGATION: A LUNAR LANDING EXAMPLE

Todd A. Ely[*] and Alexandra H. Chau[†]

The traditional role that altimetry and velocimetry have played in spacecraft landings is to provide a direct measure of the spacecraft's surface altitude and surface relative velocity; however, their role in determining an inertial position and velocity has seen limited investigation. In this study, inertially sensitive measurement models for altimetry and velocimetry are formulated that include relevant instrument and environment error models. These models are applied and simulated for a realistic lunar landing scenario that is based on recent work for NASA's Altair lander. The preliminary results indicate that inertial landing accuracies of several meters are possible.

INTRODUCTION

Navigation systems for a planetary lander often utilize altimetry and velocimetry to obtain surface relative measurements to aid with landing. These measurements play an important role typically in determining whether altitude and/or surface relative velocity constraints are being met; however, their direct use with inertial navigation has seen limited use. Since surface relative states can be related to inertial states via proper transformations it should be possible to directly estimate inertial states using altimetry and velocimetry data. The sensitivity to the inertial states introduced by these transformations should aid the inertial estimates of the vehicle and lower the overall inertial state estimate uncertainties. In turn, this will also improve the map (or landing site) relative state estimate as well.

In the present work, inertial models for the altimeter and velocimeter are developed and applied to realistic lunar landing scenarios that are based on recent work for NASA's Altair lander (References [1, 2]) and current work on the Lunar Orbit Rendezvous (LOR) lander. The resulting simulation places the altimeter and velocimeter into an on-board navigation system along with an inertial measurement unit (IMU), gimbaled passive optical camera system for landmark tracking, and Earth based ground radiometric tracking (used during the cruise and orbit mission phases and to initialize the navigation filter knowledge at the beginning of descent). Of course, any landing's success lies on the ability of the lander's navigation system to place it at a designated site which, so the effect of map tie errors are examined and how the inertial knowledge combined with camera based landmark tracking can mitigate these errors. Additionally, a model for deweighting

[*] Principal Engineer; Mission Design and Navigation Section, Jet Propulsion Laboratory, California Institute of Technology, MS 301-121, 4800 Oak Grove Drive, Pasadena, CA, 91109-8099; Todd.A.Ely@jpl.nasa.gov, 818-393-1744.

[†] Staff Engineer; Radar Science and Engineering Section, Jet Propulsion Laboratory, California Institute of Technology, MS 300-235, 4800 Oak Grove Drive, Pasadena, CA 91109-8099; Alexandra.H.Chau@jpl.nasa.gov, 818-354-0761.

altimeter data due to terrain variations using current lunar digital elevation maps (DEMs) is developed.

During Apollo, altimetry and velocimetry data from the lunar module's radar was filtered using an estimator (with empirical weighting) to improve the surface relative velocity and altitude estimates coming from the navigation system (which was just IMU inertial states transformed into surface relative states); however this data was not directly used to get full state estimates in an inertial estimator.[3] In later years, Mars robotic landers have used altimetry and velocimetry in a similar way in both real-time and off-line to aid in reconstructing the entry, descent, and landing (EDL) trajectories; though, again, the data wasn't used to improve estimates of the full inertial state.[4-6] Recent, work has begun to develop models for processing altimeter and velocimeter data in full state estimates that are fully-'fused' with the inertial state estimates coming out of the inertial measurement unit (IMU). Work by Shuang (Reference [7]) develops a fully integrated IMU, altimeter, and velocimeter model however the planet (in this case Mars) was assumed to be flat (with no terrain) and non-rotating. These assumptions eliminate some important measurement sensitivities of the state estimator that actually diminish the utility of the altimeter and velocimeter in the estimation process. Furthermore, the absence of terrain yields results that don't properly account for this effect. NASA's Autonomous Landing and Hazard Avoidance Technology (ALHAT) project has also begun investigating the use of lidar range and Doppler measurements integrated into with IMU navigation state estimates.[8] They develop a Moon centered surface-fixed estimator so the altimeter and velocimeter measurements retain their surface relative models and do not have direct sensitivity to the inertial state. However, their EOM's are expressed in a rotating coordinate frame fixed with the Moon that does introduce an indirect sensitivity to the inertial coordinates through the state transition matrix. Their work goes on to investigate different behaviors of the planet-fixed state estimator for different empirical terrain features. They conclude that the altimeter data needs to be de-weighted for these features; however their model is empirical and static. In the current work, the altimeter deweighting depends on both the lander state and terrain via scaling with changing lander position uncertainties, terrain slopes and roughness. Furthermore, the current work includes effects due DEM resolution and map-tie errors that yield more realistic performance estimates of a lunar landing navigation system.

INERITAL ALTIMETERY AND VELOCIMETERY

The fundamental finding in this work is that slant range and slant range rate measurements between an observer and rotating celestial body provide information to determine the observer's inertial state in space. Couple this information with an accurate DEM of the celestial body and the observer's location relative to the map can also be determined, in the present work the location of a lander to the desired landing site is relevant. In this analysis, the slant range and slant range rate measurements are obtained using a 6-beam Ka-band pulsed-beam radar (details to follow); however, it should be noted that the results in this work are generic and could be applied to other forms of radar, laser altimeters, lidar, etc.

Slant Range Model

To begin the analysis consider the geometry of the measurement as depicted in Figure 1, where a radar mounted on a lander measures the slant range ρ between the radar antenna and the strike point of the beam centroid on surface terrain. To actually compute this distance the intersection with the reference surface upon which a DEM overlays must be considered. In particular, this slant range ρ can be expressed using

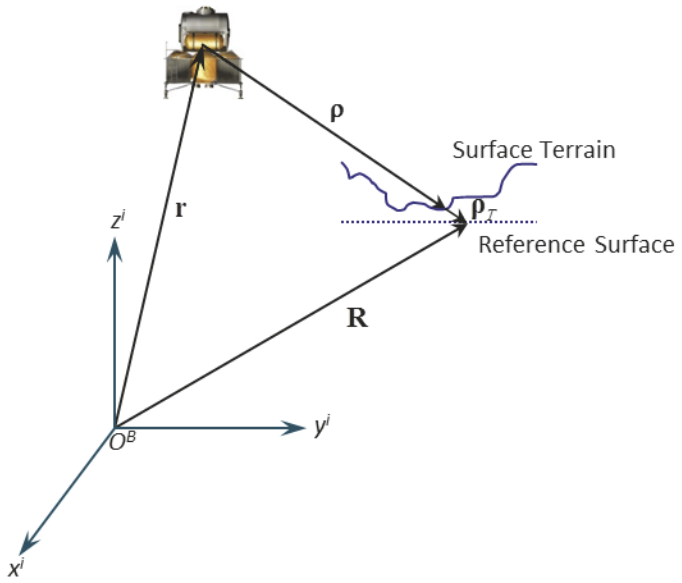

Figure 1: Geometry of a single beam slant range between a spacecraft and the surface of a central body.

$$\boldsymbol{\rho} = \mathbf{R} - \boldsymbol{\rho}_T - \mathbf{r} \quad \rightarrow \quad \rho = (\mathbf{R} - \mathbf{r}) \bullet \hat{\boldsymbol{\rho}} - \rho_T \tag{1}$$

where $\mathbf{r}$ is the position vector from the origin of the central body and the lander, $\boldsymbol{\rho} = \rho\hat{\boldsymbol{\rho}}$ is the slant range vector from the lander that ends at the radar beam centroid intersection with the surface terrain (for simplicity call this the *strike point*), $\hat{\boldsymbol{\rho}}$ is the associated unit vector, $\boldsymbol{\rho}_T = \rho_T\hat{\boldsymbol{\rho}}$ is the slant range distance from the strike point on the terrain to the intersection with the central body reference surface, and, finally, $\mathbf{R}$ is the vector from the central body origin to the intersection with the reference surface. A critical observation about $\hat{\boldsymbol{\rho}}$ is that it is known from the lander's attitude control system (ACS) and the pre-calibrated mounting of the radar antennas on the lander, thus can be considered to be independent of the two vectors $\mathbf{R}$ and $\mathbf{r}$. These vectors are placed in the context of an inertial coordinate system with axes $\{X^i, Y^i, Z^i\}$ and origin at the center of the central body O^B. Computation of ρ_T requires a DEM fixed to the reference surface which is often expressed as height h above the reference surface as a function of latitude φ and longitude λ, that is

$$h = h(\varphi, \lambda). \tag{2}$$

Slant Range Computational Algorithm: Algorithmic details for computing the sum $(\rho + \rho_T)$ then the individual components ρ and ρ_T follow:

1. Assuming the reference surface is an ellipsoid, use the line/ellipsoid intersection algorithm to solve for the sum $\rho + \rho_T$ and then $\mathbf{R}$ using $\mathbf{R} = \mathbf{r} + (\rho + \rho_T)\hat{\boldsymbol{\rho}}$ with

$$\mathbf{R}^{\mathrm{T}}\mathbf{A}\mathbf{R} = \left[\mathbf{r} + (\rho + \rho_T)\hat{\boldsymbol{\rho}}\right]^{\mathrm{T}} \mathbf{A}\left[\mathbf{r} + (\rho + \rho_T)\hat{\boldsymbol{\rho}}\right] = 1, \tag{3}$$

where $\mathbf{A} = \text{diag}\left(\frac{1}{a^2}, \frac{1}{b^2}, \frac{1}{c^2}\right)$ and $\{a, b, c\}$ are the principal axis semi-lengths of the reference ellipsoid, and the vectors are expressed in the principal axis coordinate system. It should be noted that for the Moon a reasonable shape approximation is spherical, hence $\mathbf{A}$ becomes $\mathbf{A} = \frac{1}{R^2}\mathbf{I}$ in this case. Equation (3) yields a quadratic solution for $\rho + \rho_T$ of the form

$$\rho + \rho_T = -\frac{1}{\hat{\boldsymbol{\rho}}^{\mathrm{T}}\mathbf{A}\hat{\boldsymbol{\rho}}}\left(\sqrt{\left(\mathbf{r}^{\mathrm{T}}\mathbf{A}\hat{\boldsymbol{\rho}}\right)^2 + \hat{\boldsymbol{\rho}}^{\mathrm{T}}\mathbf{A}\hat{\boldsymbol{\rho}}\left(1 - \mathbf{r}^{\mathrm{T}}\mathbf{A}\mathbf{r}\right)} + \mathbf{r}^{\mathrm{T}}\mathbf{A}\hat{\boldsymbol{\rho}}\right) \tag{4}$$

where the near side solution is negative root.

2. The solution for $\mathbf{R}$ is found with

$$\mathbf{R} = \mathbf{r} + \left(\rho + \rho_T\right)\hat{\boldsymbol{\rho}}\,. \tag{5}$$

3. The state estimate of the location of the *nominal* strike point on the reference surface defines a local topocentric coordinate system $\{\Delta x, \Delta y, \Delta z\}$ with the unit vectors $\left\{\hat{\mathbf{i}}, \hat{\mathbf{j}}, \hat{\mathbf{k}}\right\}$ and an origin O^L at latitude $\bar{\varphi}$ and longitude $\bar{\lambda}$ (the overbar refers to either a nominal value or a current filter output value) which are found via converting the Cartesian solution for $\mathbf{R}$ into geodetic coordinates.

4. Now to find ρ:

   a. Convert the lander position vector $\mathbf{r}$ and the pointing unit vector $\hat{\boldsymbol{\rho}}$ into topocentric coordinates in the topocentric frame, that is

$$\begin{aligned} \mathbf{r} &= r_{\Delta x}\hat{\mathbf{i}} + r_{\Delta y}\hat{\mathbf{j}} + r_{\Delta x}\hat{\mathbf{k}} \\ \hat{\boldsymbol{\rho}} &= \hat{\rho}_{\Delta x}\hat{\mathbf{i}} + \hat{\rho}_{\Delta y}\hat{\mathbf{j}} + \hat{\rho}_{\Delta x}\hat{\mathbf{k}} \end{aligned}\,. \tag{6}$$

   b. Convert the DEM in the region around O^L as a function of the topocentric coordinate system via converting the geodetic data $\{\varphi, \lambda, h\}$ into topocentric Cartesian data $\{\Delta x, \Delta y, h\}$.

   c. Step towards the surface along the slant range vector originating at the lander $(\mathbf{r} + \rho_i\hat{\boldsymbol{\rho}})$ where $\rho_i = \rho_{i-1} + \Delta$ with an initial guess for ρ_0 that is safely above the surface. At each step compute

$$\begin{aligned} \Delta x_i &= r_{\Delta x} + \rho_i\hat{\rho}_{\Delta x} \\ \Delta y_i &= r_{\Delta y} + \rho_i\hat{\rho}_{\Delta y} \\ \Delta z_i &= r_{\Delta z} + \rho_i\hat{\rho}_{\Delta z} \end{aligned} \tag{7}$$

   and the associated DEM height $h_i = h\left(\Delta x_i, \Delta y_i\right)$. Compare h_i with Δz_i. The stepping continues until Δz_i is below h_i, hence, bracketing the surface. The search continues using a bisection algorithm until it converges to a solution for ρ such that

$$\rho = \frac{1}{\hat{\rho}_{\Delta z}}\left(h(\Delta x, \Delta y) - r_{\Delta z}\right) \tag{8}$$

and the vector $\mathbf{r} + \rho\hat{\boldsymbol{\rho}}$ intersects the DEM.

5. Finally, ρ_T is found via differencing the results of item 1 with item 3.

From Eq. (1) it is clear that a slant range measurement is sensitive to the lander's inertial location $\mathbf{r}$, and can be used in a properly configured state estimator. However, to do this accurately requires consideration of an important stochastic effect that weights the data for variations in the terrain (which typically are not smooth differentiable functions). Consider that the formation of the nominal slant range measurement will use the filter's current estimate of the lander's inertial position and the pointing vector to compute the radar beam's nominal strike point; however, the actual radar beam strike point is somewhere else. This is illustrated in Figure 2 where the following definitions and computations are made:

1. The local topocentric coordinate system, defined earlier, with origin O^L at latitude $\bar{\varphi}$ and longitude $\bar{\lambda}$ (the overbar refers to either a nominal value or a current filter output value) represents the *nominal* strike point on the reference surface.
2. In the vicinity of this coordinate system, the local linear terrain with slope information can be obtained via sampling the DEM heights along $\{\Delta x_i, \Delta y_i\}$ to get a set of sample heights $\{h_i\}$ which can be used to least squares' fit a plane and find a local normal that conforms to

$$\mathbf{n} = \frac{\partial h}{\partial \Delta x}\hat{\mathbf{i}} + \frac{\partial h}{\partial \Delta y}\hat{\mathbf{j}} - \hat{\mathbf{k}}, \tag{9}$$

where the local slopes $\left\{\frac{\partial h}{\partial \Delta x}, \frac{\partial h}{\partial \Delta y}\right\}$ and the height of the plane at the origin of the topocentric coordinate system $\bar{h}$ are products of the fitting process. To account for the variation in the terrain over the region between the nominal strike point and the actual (unknown) strike point the sampled region is circular with a radius $R_{loc} = \sigma_{\max}$ that is the maximum uncertainty of the lander's current inertial location expressed in a surface fixed frame $\sigma_{\max}^2 = \max\left(\text{eig}\left(\mathbf{P}_{\mathbf{r}}\right)\right)$.

3. The slant range vectors $\boldsymbol{\rho}_L$ that intersect the plane (including the nominal vector $\bar{\boldsymbol{\rho}}_L$) can be found using the vector equation for a plane

$$\left(\boldsymbol{\rho}_L - \bar{h}\hat{\mathbf{k}}\right)\bullet\mathbf{n} \triangleq 0. \tag{10}$$

4. The remaining vector distance between the linear surface and the strike point (nominal, actual, or in the vicinity of O^L) is the slant range surface roughness $\boldsymbol{\rho}_R$. While the linear terrain captures smooth slopes near the nominal strike point the surface roughness is the deviation of the terrain from linearity and is not amenable to a smooth functional representation.

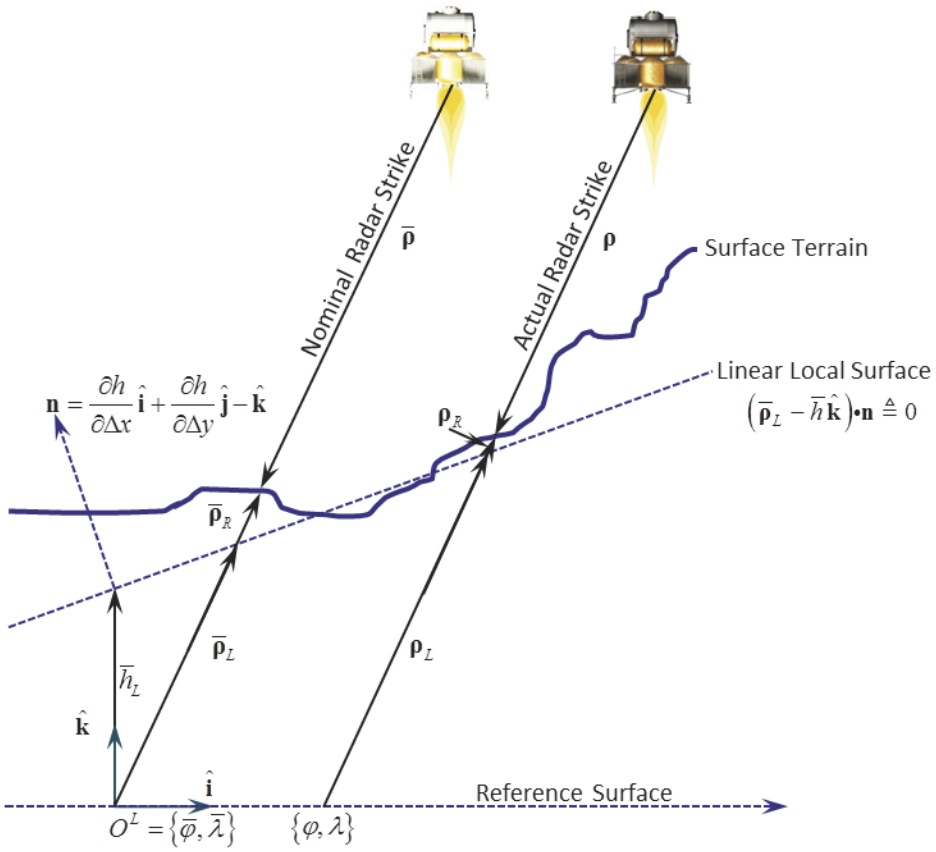

Figure 2: 2-D illustration showing the geometry of an actual radar strike point versus the one computed by the filter.

Now consider a strike point on the surface terrain, which can be the actual one or any other in the vicinity of the nominal strike point, a vector originating at O^L can be formed as the sum of two vectors that end at the associated intersection on the planar surface (i.e., excludes $\boldsymbol{\rho}_R$)

$$\mathbf{r}_L = -\rho_L\left(\hat{\boldsymbol{\rho}} + \Delta\hat{\boldsymbol{\rho}}\right) + \Delta x\hat{\mathbf{i}} + \Delta y\hat{\mathbf{j}}\,. \tag{11}$$

where $\Delta\hat{\boldsymbol{\rho}}$ is a variation in the pointing unit vector that could result from lander attitude/pointing or beam centroid errors, and $\{\Delta x, \Delta y\}$ are components of the vector from O^L to the strike point on the reference surface. Since the vector in Eq. (11) ends at the plane, it can be substituted into Eq. (10) to produce

$$\left(-\rho_L\left(\hat{\boldsymbol{\rho}} + \Delta\hat{\boldsymbol{\rho}}\right) + \Delta x\hat{\mathbf{i}} + \Delta y\hat{\mathbf{j}} - \bar{h}\hat{\mathbf{k}}\right)\bullet\left(\frac{\partial h}{\partial \Delta x}\hat{\mathbf{i}} + \frac{\partial h}{\partial \Delta y}\hat{\mathbf{j}} - \hat{\mathbf{k}}\right) \triangleq 0\,. \tag{12}$$

Manipulating this expression leads to a solution for ρ_L of the form

$$\rho_L = \frac{\bar{h} + \frac{\partial h}{\partial \Delta x}\Delta x + \frac{\partial h}{\partial \Delta y}\Delta y}{(\hat{\rho}_x + \Delta\hat{\rho}_x)\frac{\partial h}{\partial \Delta x} + (\hat{\rho}_y + \Delta\hat{\rho}_y)\frac{\partial h}{\partial \Delta y} - (\hat{\rho}_z + \Delta\hat{\rho}_z)} \tag{13}$$

where $\hat{\boldsymbol{\rho}}$ and $\Delta\hat{\boldsymbol{\rho}}$ have been resolved into components in the local topocentric frame. This equation is prescriptive in that ρ_L can be computed using the given topocentric frame, local planar surface, and specified values for $\{\Delta x, \Delta y, \Delta\hat{\rho}_x, \Delta\hat{\rho}_y, \Delta\hat{\rho}_z\}$. For a given realization of ρ_L it is now possible to compute for this radar strike the surface roughness value via $\rho_R = \rho_T - \rho_L$ where ρ_T is the slant range correction due to terrain and is computed using the algorithm given earlier. Statistics for ρ_R are generated by sampling over the local DEM in the circular region defined by $R_{loc} = \sigma_{\max}$, and can be used to deweight each slant range measurement for the terrain variability in the vicinity of the nominal strike point. To see how this is done, consider the Taylor expansion of ρ_T about the nominal strike point (which is also the expression used in the state estimator for formulating the measurement residual)

$$\rho_T = \bar{\rho}_T + \nabla_{(\Delta\mathbf{x}, \Delta\hat{\boldsymbol{\rho}})}\rho_L \bullet \begin{bmatrix} \Delta\mathbf{x} \\ \Delta\hat{\boldsymbol{\rho}} \end{bmatrix} + \delta\rho_R \tag{14}$$

and, the partials take the form

$$\nabla_{\Delta\mathbf{x}}\rho_L = \frac{1}{(\hat{\rho}_x + \Delta\hat{\rho}_x)\frac{\partial h}{\partial \Delta x} + (\hat{\rho}_y + \Delta\hat{\rho}_y)\frac{\partial h}{\partial \Delta y} - (\hat{\rho}_z + \Delta\hat{\rho}_z)} \begin{bmatrix} \frac{\partial h}{\partial \Delta x} \\ \frac{\partial h}{\partial \Delta y} \end{bmatrix}, \tag{15}$$

$$\nabla_{\Delta\hat{\boldsymbol{\rho}}}\rho_L = \frac{1}{\left[(\hat{\rho}_x + \Delta\hat{\rho}_x)\frac{\partial h}{\partial \Delta x} + (\hat{\rho}_y + \Delta\hat{\rho}_y)\frac{\partial h}{\partial \Delta y} - (\hat{\rho}_z + \Delta\hat{\rho}_z)\right]^2} \begin{bmatrix} \bar{h}\frac{\partial h}{\partial \Delta x} \\ \bar{h}\frac{\partial h}{\partial \Delta y} \\ -1 \end{bmatrix}. \tag{16}$$

The $\bar{\rho}_T$ in Eq. (14) is just the nominal value for ρ_T and is determined using the slant range computational algorithm defined earlier, the second term ($\nabla_{\Delta\mathbf{x}}\rho_L \bullet \Delta\mathbf{x} + \nabla_{\Delta\hat{\boldsymbol{\rho}}}\rho_L \bullet \Delta\hat{\boldsymbol{\rho}}$) represents a sensitivity of the measurement to the local linear surface ρ_L, and the third quantity represents the variation from the nominal ρ_R of the surface roughness in the local area. Technically, since the second term is smoothly related to the variations $\{\Delta\mathbf{x}, \Delta\hat{\boldsymbol{\rho}}\}$ via the slope information this could be used in the measurement update to aid in the solution for these quantities (via augmenting the filter vector with $\{\Delta\mathbf{x}, \Delta\hat{\boldsymbol{\rho}}\}$). However, since the slopes are generated from sample statistics they will not necessarily change smoothly and have the potential to destabilize the filter solution recursion. For now, the sensitivities in Eq. (14) will be used to define a measurement error process rather than as a path towards explicitly solving for these. Future work will investigate robust approaches for adding these terms to the filters state vector. The quantities $\{\Delta\mathbf{x}, \Delta\hat{\boldsymbol{\rho}}, \delta\rho_R\}$ can be treated as independent random variables with the following statistics:

1. The variation along the reference surface due to the actual strike point not being at the nominal point has a zero expectation $E[\Delta\mathbf{x}]=0$ because the filter is an unbiased optimal estimator. Additionally, the covariance of this variation $\mathbf{P}_{\Delta\mathbf{x}}$ is technically the projection of the lander's position covariance $\mathbf{P}_{\mathbf{r}}$ onto the reference surface. A conservative simplification is to bound $\mathbf{P}_{\Delta\mathbf{x}}$ using $\mathbf{P}_{\Delta\mathbf{x}} < \mathrm{diag}\left(\sigma_{\max}^2, \sigma_{\max}^2\right)$ where $\sigma_{\max}^2 = \max\left(\mathrm{eig}\left(\mathbf{P}_{\mathbf{r}}\right)\right)$. It should be emphasized that the uncertainty $\sigma_{\max}$ is state dependent and must be computed for each measurement using the filter's current estimate of $\mathbf{P}_{\mathbf{r}}$.

2. The present study is 3-DOF and estimates lander position and velocity. The landers attitude and pointing is handled in the filter using a representative stochastic noise process. Analysis of the attitude estimation process indicates that the attitude uncertainty is bounded and relatively static via use of stable rate gyro's and frequent (every 10 second) attitude fixes using the lander's star trackers. These attitude and pointing noise processes are characterized later in this paper. Presently, for the terrain variability statistics calculations the pointing error is modeled as a simple unestimated random variable with $E[\Delta\hat{\boldsymbol{\rho}}]=0, \quad \mathbf{P}_{\Delta\hat{\boldsymbol{\rho}}} = E\left[\Delta\hat{\boldsymbol{\rho}}\Delta\hat{\boldsymbol{\rho}}^{\mathrm{T}}\right] = diag(\sigma_{\hat{\rho}}^2, \sigma_{\hat{\rho}}^2, \sigma_{\hat{\rho}}^2)$.

3. In this study the Lunar Orbiter Laser Altimeter (LOLA) DEM produced by the Lunar Reconnaissance Orbiter (LRO) (Reference [9]) has been utilized to formulate sample statistics for the local slope $\nabla_{\Delta\mathbf{x}}h$ and surface roughness along the lander's trajectory with $E[\delta\rho_R]=0$ by definition of the linear planar surface and $\sigma_R = \sqrt{E\left[\delta\rho_R^2\right]}$ is the standard deviation of the fitting process for the plane. The sampling of the terrain statistics is limited by the DEM resolution R_{DEM}, so for $R_{\mathrm{loc}} < R_{\mathrm{DEM}}$ the sample statistics for $\delta\rho_R$ at R_{DEM} have been selected to scale linearly such that they approach zero as $R_{\mathrm{loc}} \downarrow 0$.

Using the preceding statistics the sum $\nabla_{(\Delta\mathbf{x},\Delta\hat{\boldsymbol{\rho}})}\rho_L \bullet \begin{bmatrix}\Delta\mathbf{x}\\ \Delta\hat{\boldsymbol{\rho}}\end{bmatrix} + \delta\rho_R$ in Eq. (14) has the following property for its mean value

$$E\left[\nabla_{\Delta\mathbf{x}}\rho_L \bullet \Delta\mathbf{x} + \nabla_{\Delta\hat{\boldsymbol{\rho}}}\rho_L \bullet \Delta\hat{\boldsymbol{\rho}} + \delta\rho_R\right] = E\left[\nabla_{\Delta\mathbf{x}}\rho_L\right]\bullet\mathbf{0} + E\left[\nabla_{\Delta\hat{\boldsymbol{\rho}}}\rho_L\right]\bullet\mathbf{0} + 0 = 0, \tag{17}$$

and associated covariance

$$\begin{aligned} E\left[\left(\nabla_{\Delta\mathbf{x}}\rho_L \bullet \Delta\mathbf{x} + \nabla_{\Delta\hat{\boldsymbol{\rho}}}\rho_L \bullet \Delta\hat{\boldsymbol{\rho}} + \delta\rho_R\right)^2\right] &= E\left[\nabla_{\Delta\mathbf{x}}\rho_L\right]^{\mathrm{T}}\mathbf{P}_{\Delta\mathbf{x}}E\left[\nabla_{\Delta\mathbf{x}}\rho_L\right] + E\left[\nabla_{\Delta\hat{\boldsymbol{\rho}}}\rho_L\right]^{\mathrm{T}}\mathbf{P}_{\Delta\hat{\boldsymbol{\rho}}}E\left[\nabla_{\Delta\hat{\boldsymbol{\rho}}}\rho_L\right] + \sigma_R^2 \\ &< \sigma_{\max}^2\nabla_{\Delta\mathbf{x}}\rho_L \bullet \nabla_{\Delta\mathbf{x}}\rho_L + \sigma_{\hat{\rho}}^2\nabla_{\Delta\hat{\boldsymbol{\rho}}}\rho_L \bullet \nabla_{\Delta\hat{\boldsymbol{\rho}}}\rho_L + \sigma_R^2. \end{aligned} \tag{18}$$

These statistics can be used to drive an appropriate state dependent stochastic process to deweight each slant range measurement where the covariance in Eq. (18) is the noise strength of the process. To better expose this error source for deweighting the slant range model given in Eq. (1) it is modified to explicitly include $\{\Delta\mathbf{x}, \Delta\hat{\boldsymbol{\rho}}, \delta\rho_R\}$ as zero mean random variables with statistics previously discussed, that is

$$\rho = (\mathbf{R}-\mathbf{r})\bullet\hat{\boldsymbol{\rho}} - \rho_T - \nabla_{(\Delta\mathbf{x},\Delta\hat{\boldsymbol{\rho}})}\rho_L \bullet \begin{bmatrix}\Delta\mathbf{x}\\ \Delta\hat{\boldsymbol{\rho}}\end{bmatrix} - \delta\rho_R. \tag{19}$$

where the overbar on ρ_T has been dropped because its computation is understood to follow previously given algorithm. Eq. (19) represents a useful stochastic model that makes explicit the terrain error sources contributing to the slant range.

Single Beam Nadir Case: At the time of this writing the full implementation of the 6-beam slant range radar model is still being developed. The slant range terrain variability plug-in has been developed, but needs to be integrated. As a proof-of-concept a single beam nadir pointed altimeter measurement model has been implemented and has been used to generate the simulation results presented in this paper. The preceding concepts developed for an arbitrarily pointed slant range measurement still apply except now the slant range expression in Eq. (19) reduces for a spherical body to the following stochastic altitude measurement

$$\rho = r - R - \rho_T - \nabla_{(\Delta\mathbf{x},\Delta\hat{\boldsymbol{\rho}})}\rho_L \bullet \begin{bmatrix} \Delta\mathbf{x} \\ \Delta\hat{\boldsymbol{\rho}} \end{bmatrix} - \delta\rho_R \quad \text{(nadir)} \tag{20}$$

The expression for ρ_L reduces to

$$\begin{aligned} \rho_L &= \frac{\bar{h} + \dfrac{\partial h}{\partial \Delta x}\Delta x + \dfrac{\partial h}{\partial \Delta y}\Delta y}{\Delta\hat{\rho}_x \dfrac{\partial h}{\partial \Delta x} + \Delta\hat{\rho}_y \dfrac{\partial h}{\partial \Delta y} + \left(1 - \Delta\hat{\rho}_z\right)} \\ &= \bar{h}\left(1 + \Delta\hat{\rho}_z\right) + \frac{\partial h}{\partial \Delta x}\left(\Delta x - \bar{h}\Delta\hat{\rho}_x\right) + \frac{\partial h}{\partial \Delta y}\left(\Delta y - \bar{h}\Delta\hat{\rho}_y\right) + O\left(\Delta^2\right). \end{aligned} \tag{21}$$

Consider a nutation error $\delta\theta$ in pointing with an arbitrary azimuth leads to

$$\Delta\hat{\boldsymbol{\rho}} = \cos\psi \sin\delta\theta\hat{\mathbf{i}} + \sin\psi \sin\delta\theta\hat{\mathbf{j}} - \cos\theta\hat{\mathbf{k}} < \frac{\delta\theta}{\sqrt{2}}\hat{\mathbf{i}} + \frac{\delta\theta}{\sqrt{2}}\hat{\mathbf{j}} + O\left(\delta\theta^2\right) \tag{22}$$

with the following result on Eq. (21)

$$\begin{aligned} \rho_L &= \bar{h} + \frac{\partial h}{\partial \Delta x}\left(\Delta x - \frac{\bar{h}\delta\theta}{\sqrt{2}}\right) + \frac{\partial h}{\partial \Delta y}\left(\Delta y - \frac{\bar{h}\delta\theta}{\sqrt{2}}\right) + O\left(\Delta^2\right) \\ &= \bar{h} + \frac{\partial h}{\partial \Delta x}\Delta x' + \frac{\partial h}{\partial \Delta y}\Delta y' + O\left(\Delta^2\right). \end{aligned} \tag{23}$$

where $\Delta x' \triangleq \Delta x - \dfrac{\bar{h}\delta\theta}{\sqrt{2}}$ and $\Delta y' \triangleq \Delta x - \dfrac{\bar{h}\delta\theta}{\sqrt{2}}$. The appearance of $\Delta x'$ and $\Delta y'$ has lumped the effect of the pointing error into the local terrain sample statistics calculations via redefining the radius of the sampling region to be

$$R_{loc} = \sqrt{\sigma_{\max}^2 + \bar{h}\sigma_{\hat{\rho}}^2} \tag{24}$$

Using the preceding facts the terrain partials take the form

$$\nabla_{\Delta\mathbf{x}'}\rho_L = \begin{bmatrix} \dfrac{\partial h}{\partial \Delta x} \\ \dfrac{\partial h}{\partial \Delta y} \end{bmatrix}. \tag{25}$$

Finally, given this rescaling, Eq. (20) is recast as

$$\rho = r - R - \rho_T - \frac{\partial h}{\partial \Delta x'}\Delta x' - \frac{\partial h}{\partial \Delta y'}\Delta y' - \delta\rho_R \quad \text{(nadir)} . \tag{26}$$

The seeming de-emphasis on pointing error for the case of the nadir pointed beam will become evident later where it is shown that the altitude measurement is insensitive to pointing error at first order.

Slant Range Rate Model

The radar velocimeter measures the slant range rate velocity of each beam. The general case of a multi-beam velocimeter is developed, and, for this work the 6-beam model velocimeter has been developed with the results reported here. To begin consider a single beam, its slant range rate is defined as

$$\frac{d\rho}{dt} = \frac{d}{dt}\left[(\mathbf{R}-\mathbf{r})\bullet\hat{\boldsymbol{\rho}} - \Delta\boldsymbol{\rho}_T\bullet\hat{\boldsymbol{\rho}}\right] = \left(\frac{d\mathbf{R}}{dt} - \frac{d\Delta\boldsymbol{\rho}_T}{dt} - \mathbf{v}\right)\bullet\hat{\boldsymbol{\rho}} \tag{27}$$

where the time differentiation is inertial and $\mathbf{v} \triangleq d\mathbf{r}/dt$. Since the terrain is rigidly fixed to the reference surface, and the central body is considered to rotate rigidly the inertial velocity of the first two terms in Eq. (27) are given by

$$\frac{d\mathbf{R}}{dt} - \frac{d\Delta\boldsymbol{\rho}_T}{dt} = \boldsymbol{\omega}\times(\mathbf{R}-\Delta\boldsymbol{\rho}_T) = \boldsymbol{\omega}\times(\mathbf{r}-\boldsymbol{\rho}) \tag{28}$$

where $\boldsymbol{\omega}$ is the angular velocity of the central body. Substituting Eq. (28) into Eq. (27) and manipulating yields

$$\frac{d\rho}{dt} = \left(\boldsymbol{\omega}\times(\mathbf{r}-\boldsymbol{\rho}) - \mathbf{v}\right)\bullet\hat{\boldsymbol{\rho}} = (\boldsymbol{\omega}\times\mathbf{r} - \mathbf{v})\bullet\hat{\boldsymbol{\rho}} . \tag{29}$$

The final expression in Eq. (29) is obtained using the identity $(\boldsymbol{\omega}\times\boldsymbol{\rho})\bullet\boldsymbol{\rho} = 0$, thus indicating that the slant range rate is independent of the terrain (actual and reference) and depends only on the inertial position and velocity of the lander and the radar pointing vector. This is a fundamental result that, as will be shown, has a profound effect on the use of velocimeter for inertial navigation. Indeed, unlike the altimeter there is no required deweighting due to terrain variations.

Radar Altimeter and Velocimeter Models

The preceding work on slant range and slant range rate measurements can now be put into the context of a realistic radar model. These models are based on using a Ka-band pulsed-beam radar that has been included in the conceptual design for NASA's Altair and LOR lander navigation system designs. This is the same radar that is being used by the landing system of the Mars Science Laboratory (MSL) rover that will launch in the Fall of 2011.[10] It is illustrated in Figure 3. The radar has six beams that combine to form a measurement of the altitude on a nominal 20 Hz rate. The beams can form slant range measurements if the range to the surface is less than some maximum value. For the MSL version of the radar this is nominally 12 km but can be extended to 20 km at a reduced measurement rate (this will be done in the current research). The velocimeter is activated when the surface relative speed is less than a maximum value (for the MSL radar this ±210 m/s).

To resolve the vector expressions for slant range (Eq. (14)) and slant range rate (Eq. (29)) and their associated partials it is necessary to put the vectors into consistent coordinate systems. Re-

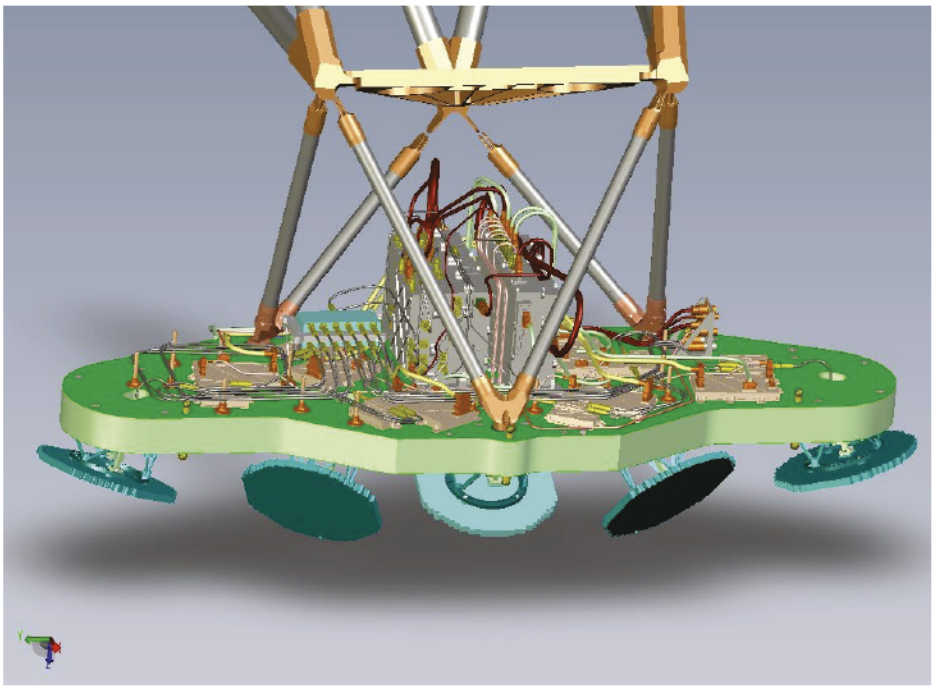

Figure 3: Radar with electronics showing 5 of the 6 antennas.

call, that the intent of processing these measurements is to determine the lander's state in inertial space (and ultimately map relative states) therefore slant range and slant range rate measurements taken in a lander fixed frame (also the GNC frame) need to be related to the inertial frame. The lander fixed (*lf*) frame and the radar antenna (and associated beam alignments) are illustrated in Figure 4. The lander fixed frame is defined with X (yaw), Y (pitch), and Z (roll). This frame is related to the inertial (*i*) frame via the rotation

$$\mathbf{T}_i^{lf} = \text{rotation from the inertial frame to the lander fixed frame} \quad \rightarrow \quad \mathbf{x}^{lf} = \mathbf{T}_i^{lf}\mathbf{x}^i \qquad (30)$$

The radar is mounted at the base of the lander with the base plate of the radar in the ZY-plane. The beams are oriented such that they generally point in the –Z and –X directions (back and down with a vertically oriented lander). There are 6 beams in total with elevation δ angle (defined with respect to the –X axis with positive angle towards –Z) and azimuth angle ϕ (defined with respect to the –Z axis with positive angle towards +Y) defining the pointing direction relative to the lander fixed frame. Specifically, each beam's pointing vector takes the form

$$\hat{\boldsymbol{\rho}} = -\cos\phi\cos\delta\hat{\mathbf{i}}^{lf} + \sin\phi\cos\delta\hat{\mathbf{j}}^{lf} - \sin\delta\hat{\mathbf{k}}^{lf} \qquad (31)$$

where $\left\{\hat{\mathbf{i}}^{lf}, \hat{\mathbf{j}}^{lf}, \hat{\mathbf{k}}^{lf}\right\}$ are the unit vectors aligned with the lander fixed frame axes $\left\{X^{lf}, Y^{lf}, Z^{lf}\right\}$, respectively. The orientation of each beam is given in Table 1.

Table 1: Orientation Angles of Each Radar Beam

	Elevation Angle δ	Azimuth Angle ϕ
Nadir Beam 1	0°	0°
Nadir Beam 2	0°	0°

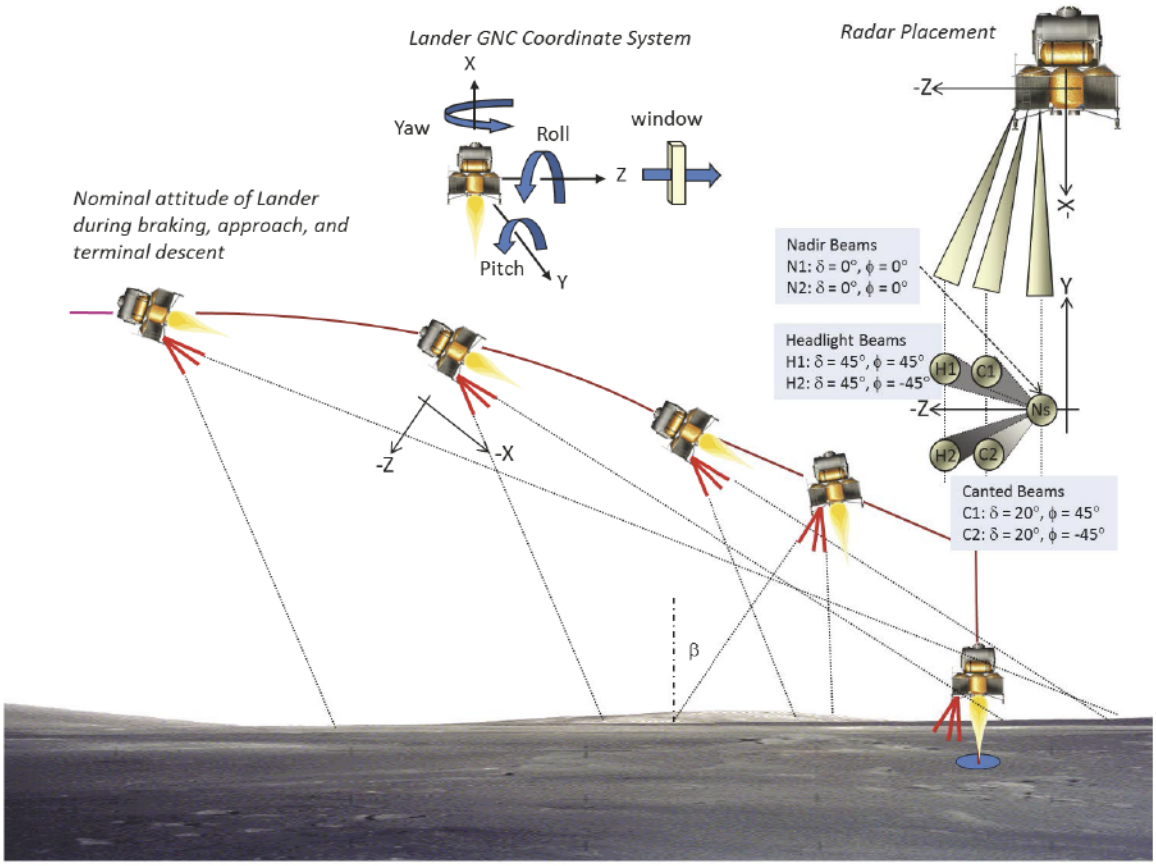

Figure 4: Lander coordinate system, radar placement with respect to this system, and the nominal attitude during powered descent showing the envelope of radar beam incidence angles.

Canted Beam 1	20°	45°
Canted Beam 2	20°	-45°
Headlight Beam 1	45°	45°
Headlight Beam 2	45	-45°

A complete model for the slant range and slant range rate can now be formulated in inertial coordinates.

Multi-Beam Slant Range Altimeter[*]: It is convenient to convert the vector arithmetic expressions for the slant range in Eq. (1) into matrix form with the result

$$\rho = \left[\hat{\boldsymbol{\rho}}^{lf}\right]^{\mathrm{T}} \mathbf{T}_i^{lf} \left(\mathbf{R} - \mathbf{r}\right) - \left(\rho_L + \rho_R\right) \tag{32}$$

[*] Even though the radar is measuring a slant range between the lander and the surface, it is traditional to still refer to the identify this use of the radar as an altimeter.

where $\hat{\boldsymbol{\rho}}^{lf} = \left[-\cos\phi\cos\delta, \sin\phi\cos\delta, \sin\delta\right]^{\mathrm{T}}$ and the transformation $\mathbf{T}_i^{lf}$ carries the pointing vector into the inertial frame, additionally the vectors $\mathbf{R}$ and $\mathbf{r}$ are expressed in inertial coordinates. The expression in Eq. (32) is now embedded in a model for the radar slant range measurement for beam j that includes the relevant error sources

$$\rho_j^{alt} = s_j^{alt}\left\{\left[\hat{\boldsymbol{\rho}}_j^{lf} + \frac{\partial\hat{\boldsymbol{\rho}}_j^{lf}}{\partial\boldsymbol{\xi}}\Delta\boldsymbol{\xi}_j\right]^{\mathrm{T}}\mathbf{T}_i^{lf}\left[\mathbf{I}+\left[\Delta\boldsymbol{\varepsilon}\right]_s\right]\left(\mathbf{R}_j-\mathbf{r}\right) - \rho_{T,j} - \nabla_{(\Delta\mathbf{x},\Delta\hat{\boldsymbol{\rho}})}\rho_{L,j}\bullet\begin{bmatrix}\Delta\mathbf{x}_j\\ \Delta\hat{\boldsymbol{\rho}}_j\end{bmatrix} - \delta\rho_{R,j} + b_j^{alt}\right\} + \upsilon_j^{alt} \quad (33)$$

where s_j^{alt} is the scale factor, $\Delta\boldsymbol{\xi}_j = \left[\Delta\phi_j, \Delta\delta_j\right]^{\mathrm{T}}$ are the pointing errors of the beam, $\Delta\boldsymbol{\varepsilon} = \left[\Delta\varepsilon_x, \Delta\varepsilon_y, \Delta\varepsilon_z\right]^{\mathrm{T}}$ are the lander attitude errors along $\left\{X^{lf}, Y^{lf}, Z^{lf}\right\}$, b_j^{alt} is the bias, and υ_j^{alt} is the measurement noise, which is a function of the slant range of the measurement. Recall, that $\left\{\Delta\mathbf{x}_j, \Delta\hat{\boldsymbol{\rho}}_j, \delta\rho_{R,j}\right\}$ (the appearance of the subscript j is to emphasize that the statistics are computed on a per-beam basis) are being treated as independent random variables that will be used to de-weight the slant range measurement along with the measurement noise υ_j^{alt}. Note that $\frac{\partial\hat{\boldsymbol{\rho}}_j^{lf}}{\partial\boldsymbol{\xi}}$ takes the form

$$\frac{\partial\hat{\boldsymbol{\rho}}^{lf}}{\partial\boldsymbol{\xi}} = \begin{bmatrix}\sin\phi_j\cos\delta_j & \cos\lambda_j\sin\delta_j\\ \cos\phi_j\cos\delta_j & -\cos\lambda_j\sin\delta\\ 0 & -\cos\delta_j\end{bmatrix}, \quad (34)$$

and $\left[\Delta\boldsymbol{\varepsilon}\right]_s$ is the following skew symmetric matrix

$$\left[\Delta\boldsymbol{\varepsilon}\right]_s = \begin{bmatrix}0 & \Delta\varepsilon_z & -\Delta\varepsilon_y\\ -\Delta\varepsilon_z & 0 & \Delta\varepsilon_x\\ \Delta\varepsilon_y & -\Delta\varepsilon_x & 0\end{bmatrix}. \quad (35)$$

Now the state estimator incorporating measurements conforming to Eq. (33) will include $\left\{\mathbf{r}, s_j^{alt}, b_j^{alt}, \Delta\boldsymbol{\xi}_j, \Delta\boldsymbol{\varepsilon}\right\}$ in the filter state vector. Partials of Eq. (33) with respect to these quantities are needed for the filtering. However, these are straightforward and for the sake of brevity won't be provided. Using the prior discussion on the terrain variability statistics, the noise strength for the measurement noise is

$$\sigma_j^{alt} = \sqrt{\sigma_{\max}^2\nabla_{\Delta\mathbf{x}}\rho_{L,j}\bullet\nabla_{\Delta\mathbf{x}}\rho_{L,j} + \sigma_{\hat{\rho}}^2\nabla_{\Delta\hat{\boldsymbol{\rho}}}\rho_{L,j}\bullet\nabla_{\Delta\hat{\boldsymbol{\rho}}}\rho_{L,j} + \sigma_{R,j}^2 + \sigma_{noise}^2}\,. \quad (36)$$

Observe, that this is state-dependent on the filter's current state uncertainties, the lander's current location, the local terrain, and the value of the slant range.

Single Beam Nadir Altimeter: For the single beam nadir pointed case a simpler expression can be obtained by starting with a model where the pointing error $\Delta\hat{\boldsymbol{\rho}}$ has been made explicit via expanding Eq. (26) about $\hat{\boldsymbol{\rho}}$ and then embedding into a physical model with the other relevant beam errors

$$\rho_{nadir}^{alt} = s^{alt}\left\{r - R + \frac{(r-R)}{R}\mathbf{r}\bullet\Delta\hat{\boldsymbol{\rho}} - \rho_T - \frac{\partial h}{\partial \Delta x'}\Delta x' - \frac{\partial h}{\partial \Delta y'}\Delta y' - \delta\rho_R + b^{alt}\right\} + \upsilon^{alt}. \tag{37}$$

Observe that a nadir pointed beam rigidly fixed to the lander leads to the conclusion $\hat{\mathbf{i}}^{lf} = \hat{\mathbf{r}}$, and, using Eq. (34),

$$\mathbf{r}\bullet\Delta\hat{\boldsymbol{\rho}} = r\hat{\mathbf{i}}^{lf}\bullet\left(\Delta\phi\hat{\mathbf{j}}^{lf} - \Delta\delta\hat{\mathbf{k}}^{lf}\right) = 0. \tag{38}$$

This indicates that a nadir pointed altimeter beam is insensitive to pointing error *to first order*. Indeed, a higher order expansion reveals that pointing errors would be included beginning with second order terms containing $\Delta\hat{\boldsymbol{\rho}}\Delta\hat{\boldsymbol{\rho}}^{\mathrm{T}}$. Since the current analysis utilizes linear filtering, the final result for a single beam nadir pointed altimeter measurement can be simply expressed using

$$\rho_{nadir}^{alt} = s^{alt}\left\{r - R - \rho_T - \frac{\partial h}{\partial \Delta x'}\Delta x' - \frac{\partial h}{\partial \Delta y'}\Delta y' - \delta\rho_R + b^{alt}\right\} + \upsilon^{alt}. \tag{39}$$

Now the state estimator incorporating measurements conforming to Eq. (39) will include $\left\{\mathbf{r}, s^{alt}, b^{alt}\right\}$ in the filter state vector. Again, the partials are straightforward and for the sake of brevity won't be provided. The de-weighting strength for the measurement is

$$\sigma_{nadir}^{alt} = \sqrt{\sigma_{\max}^2\left[\left(\frac{\partial h}{\partial \Delta x'}\right)^2 + \left(\frac{\partial h}{\partial \Delta y'}\right)^2\right] + \sigma_R^2 + \sigma_{noise}^2}. \tag{40}$$

Multi-Beam Slant Range Rate Velocimeter: Turning to the slant range rate measurements by each radar beam, convert the expression in Eq. (29) into matrix form with the result

$$\frac{d\rho}{dt} = \left[\hat{\boldsymbol{\rho}}^{lf}\right]^{\mathrm{T}}\mathbf{T}_i^{lf}\left(\left[\boldsymbol{\omega}\right]_{\times}\mathbf{r} - \mathbf{v}\right) \tag{41}$$

with the skew symmetric angular velocity cross product matrix $\left[\boldsymbol{\omega}\right]_{\times}$ defined as

$$\left[\boldsymbol{\omega}\right]_{\times} = \begin{bmatrix} 0 & -\omega_z & \omega_y \\ \omega_z & 0 & -\omega_x \\ -\omega_y & \omega_x & 0 \end{bmatrix} \tag{42}$$

and $\{\boldsymbol{\omega}, \mathbf{r}, \mathbf{v}\}$ have been resolved in inertial components. Note that the signs on $\left[\boldsymbol{\omega}\right]_{\times}$ are reversed from $\left[\Delta\boldsymbol{\varepsilon}\right]_s$, which results from the first being associated with an active rotation while the second is a passive one. The expression in Eq. (41) is now embedded in a model for the radar slant range rate measurement for beam j that includes the relevant error sources

$$\frac{d\rho_j^{vel}}{dt} = s_j^{vel}\left\{\left[\hat{\boldsymbol{\rho}}_j^{lf} + \frac{\partial\hat{\boldsymbol{\rho}}_j^{lf}}{\partial\boldsymbol{\xi}}\Delta\boldsymbol{\xi}_j\right]^{\mathrm{T}}\mathbf{T}_i^{lf}\left[\mathbf{I} + \left[\Delta\boldsymbol{\varepsilon}\right]_s\right]\left(\left[\boldsymbol{\omega}\right]_{\times}\mathbf{r} - \mathbf{v}\right) + b_j^{vel}\right\} + \upsilon_j^{vel}, \tag{43}$$

where s_j^{vel} is the scale factor, $\Delta\boldsymbol{\xi}_j = \left[\Delta\phi_j, \Delta\delta_j\right]^{\mathrm{T}}$ are the pointing errors of the beam, $\Delta\boldsymbol{\varepsilon} = \left[\Delta\varepsilon_x, \Delta\varepsilon_y, \Delta\varepsilon_z\right]^{\mathrm{T}}$ are the lander attitude errors along $\left\{X^{lf}, Y^{lf}, Z^{lf}\right\}$, b_j^{vel} is the bias, and υ_j^{vel} is the measurement noise which, unlike the altimeter, is *not* a function of the slant range (or even

the slant range rate). A significant difference with the velocimeter measurement compared to the altimeter measurement is that there is no dependency on the terrain; it is purely a function of the vehicle inertial state and attitude. The state estimator incorporating measurements conforming to Eq. (43) will include $\{\mathbf{r}, \mathbf{v}, s_j^{vel}, b_j^{vel}, \Delta\xi_j, \Delta\boldsymbol{\varepsilon}\}$ in the filter state vector. While it is true that the central body's angular velocity $\boldsymbol{\omega}$ appears in Eq. (43); for the Moon its known sufficiently well that it is not a significant error source in determining the lander's inertial position or velocity.[11]

LANDER NAVIGATION SYSTEM AND COVARIANCE STUDY SETUP

Covariance studies of a realistic lunar landing navigation system using the radar based altimeter and velocimeter measurements, just presented, as well as other navigation instruments such as an inertial measurement unit (IMU) and a gimbaled passive optical camera for landmark tracking will be investigated. In particular, the navigation system is based on recent work for NASA's Altair lander and current work on a Lunar Orbit Rendezvous (LOR) lander. The navigation system for Altair was described in detail by Ely (Reference [1]) which investigated Altair's navigation performance during the trans-lunar cruise, lunar orbit, and descent/landing mission phases. In the present work two different trajectories will be examined in the lunar orbit and descent/landing phases:

1. A Lunar South Pole landing at Shackleton crater that is based on Altair's design reference mission
2. A Lunar Equatorial landing that is based on the LOR lander design reference mission

The purpose of analyzing the lunar orbit phase is to be able to properly initialize the navigation filter starting conditions at the beginning of powered descent.

Design Reference Mission (DRM) Descriptions

In either of these cases about 24 hours prior to Powered Descent Initiation (PDI) the lander will be mated with the Multi-Purpose Crew Vehicle (MPCV) and loitering in a ~2 hr polar 100 km x 100 km altitude parking orbit. Separation from the MPCV begins at about 2.5 orbital revolutions prior to the PDI with the MPCV performing the separation maneuver. At ½ rev prior to PDI the final in-orbit maneuver, called the De-Orbit Insertion (DOI), occurs and places the lander in a 100 km x 15.24 km altitude transfer orbit. At perilune of this orbit (i.e. at a 15.24 km altitude), the lander initiates the landing sequence consisting of three main sequences the Braking Phase/Pitch-Up, Approach Phase, and Terminal Descent (these are notionally illustrated in Figure 2). All of these phases require fully closed-loop navigation guided burns. The Braking Phase of descent is used as the primary deceleration phase where most of the vehicle's kinetic energy is burned off. The attitude is primarily horizontal with the thrust vector opposite the velocity vector. At the end of this phase the vehicle performs an attitude change to have the thrust vector pointed upward along a line that has a 10° angle from vertical. This attitude allows for improved visualization of the approach to landing, assessment of hazards, and, if necessary, re-designation of the landing site to somewhere nearby to avoid hazards. The Terminal phase is the final one and is a vertical descent beginning 100 m off of the surface; it begins with a nearly zero horizontal and a constant vertical descent velocity of 1 m/s and ends at touchdown.

Navigation System and Covariance Study Description

The lander navigation sensor suite is now described and a navigation performance simulation tool has been constructed using models for the navigation sensors and associated errors, the DRMs and associated environment/vehicle errors, and the underlying operational concept (i.e., duty cycles, critical event times, etc). In the description that follows the sensors are briefly de-

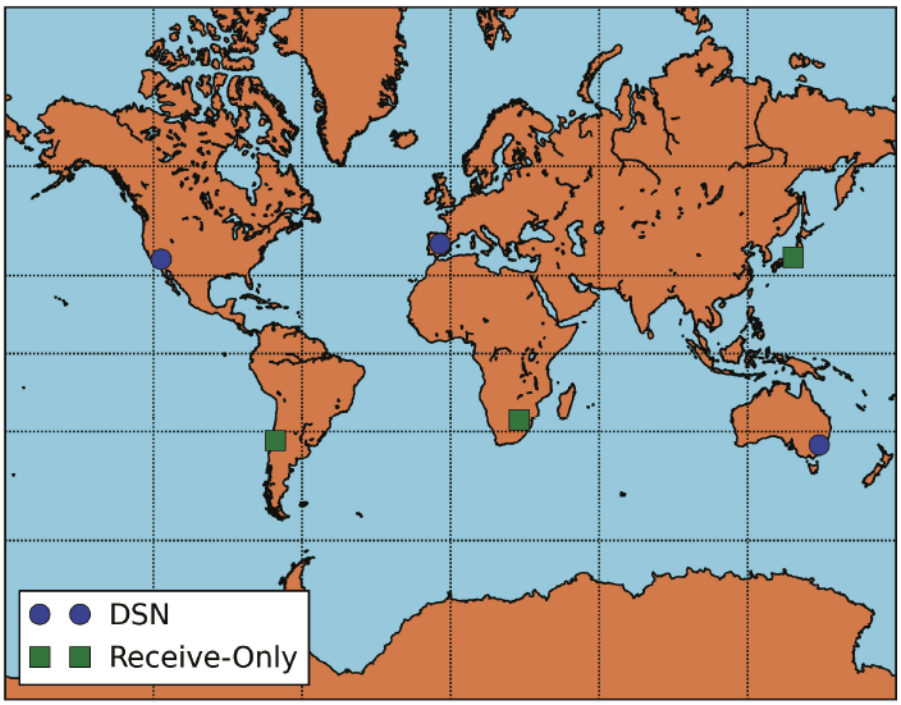

Figure 5: Earth-Based Ground Network complex locations.

scribed and their associated filter error parameters are provided in accompanying tables. Details on the vehicle and environment model and errors are described in Ely (Reference [1]) and for completeness the filter parameters associated with these models are provided in the tables in Appendix A.

Radar Altimeter and Velocimeter: The mathematical models identified earlier have been implemented in the navigation simulation for the single beam nadir pointed altimeter and the 6-beam slant range based velocimeter. The associated sensor performance parameters and their associated filter models are defined in Table 2. Recall that the primary operational envelope for the altimeter begins when the slant range to the surface is less than 12 km, in this region the al-

Table 2: Altimeter and Velocimeter Performance Parameters (per Beam)

Error Source	Parameter Type	A Priori Uncertainty (1σ)	Correlation Time / Distance
Altimeter Scale Factor Uncertainty	1st-Order Gauss–Markov	0.10%	100 s
Altimeter Bias Uncertainty	1st-Order Gauss–Markov	0.1 m	100 s
Altimeter Measurement Noise	-	2%	-
Velocimeter Scale Factor Uncertainty	1st-Order Gauss–Markov	0.13%	100 s
Velocimeter Bias Uncertainty	1st-Order Gauss–Markov	0.01 m/s	100 s
Velocimeter Measurement Noise	-	0.16 m/s	-
Beam Centroid and Radar Antenna Alignment	Estimate Random Bias	0.1° azimuth 0.1° elevation	-

timeter collects data at a 20 Hz rate with the error characteristics described in the remainder of the table. In the outer operational envelope where the slant ranges are less than 20 km the rate of successful measurements scales between 60% of 20 Hz at 20 km to 100% at 12 km, but the error characteristics remain the same.[10] As a first approximation to this behavior the measurement rate f scaling takes the form

$$f = \begin{cases} 20\ \text{Hz}, & r < 12\ \text{km}, \\ 20\ \text{Hz}\left[1 - \dfrac{1-.6}{20\ \text{km} - 12\ \text{km}}\left(r - 12\ \text{km}\right)\right], & 12\ \text{km} < r < 20\ \text{km}. \end{cases} \tag{44}$$

MSL field tests of the radar have shown the scaling is not quite linear but is adequate for an initial study. The velocimeter becomes active when the surface relative velocity is below 210 m/s, once this is true the velocimeter data collection rate is 20 Hz. For both the South Pole and Equatorial lander the velocimeter doesn't become active until the altitude is below about 2 km, hence when the lander is in the vicinity of the landing site.

Radiometric Tracking: During lunar orbit, navigation is ground based with primary tracking data coming from the Earth Based Ground System (EBGS). The radiometric tracking data consists of 2-Way Doppler and range to the Deep Space Network (DSN) and 3-Way Doppler to additional receive-only stations. The EBGS consists of the DSN with complexes located at Goldstone in California, Madrid in Spain, and Canberra in Australia, and three receive-only stations located at Santiago in Chile, Hartebeesthoek in South Africa, and Usuda in Japan. These locations are shown in Figure 5. Tracking to by stations occurs when there is a line-of-sight to the lander above a 10° elevation angle with measurements being taken every 60 seconds until about 10 minutes prior to PDI. Error characteristics of the EBGS radiometric tracking data are provided in Table 4.

Optical Landmark Tracking: The radiometric data is the nominal data type needed to determine the lunar orbit; however, in addition to this the lander also has a gimbaled dual head camera system that is used to track lunar landmarks that can also be used to determine the trajectory during orbit and descent/landing. Prior to descent, imaging with the camera system is used primarily for navigation in the event of loss of ground support, however for descent and landing it is necessary for achieving a precision landing. The gimbal has 2-degrees of freedom (2-DOF) with a wide angle 20° field of view camera (WAC) and a narrow angle 1.4° FOV camera (NAC) mounted on it. Details on the camera system and its use for navigation are provided in Riedel (Reference [12]) and Ely (Reference [1]). Even though the focus of this work is on the altimeter and velocimeter results using the gimbaled op-nav camera system have been included for completeness. To this end, the camera system will track 10-15 landmarks per picture frame. During lunar orbit pictures are taken every 10 minutes by both cameras and during descent only the WAC is imaging at a 5 second frequency. The data is cut-off at 10 m above the landing site. Error characteristics of the camera system are provided in Table 3.

Table 4: EBGS radiometric tracking errors and station location uncertainties

Error Source	Filter Parameter Type	A Priori Uncertainty (1σ)	Update Time	Reasoning/Comments
S-Band 2/3-way Doppler Noise	–	0.674 mm/s @ 60 sec	–	RSS of 1 mm/s @ 60 s (3σ) for the EBGS and 0.3 mm/s @ 60 s (3 s) for s/c transponder
S-Band 3-Way Doppler Bias	Estimate Random Bias	0.3 mm/s	Per pass	Allan Deviation at 1e-13/day yields an equivalent of 0.03 mm/s - 0.1 mm/s represents a conservative bound
S-Band 2-way Range Noise	–	6.5 ns (~ 1.95 m)	–	RSS of 4.5 m@60 s (3 σ) for the EBGS and 4.5 m@60 s (3σ) for s/c transponder.
S-Band 2-Way Range Bias	Estimate Random Bias	6.5 ns (~ 1.95 m)	Per pass	RSS of 9 m (3σ) for the EBGS and 9 m (3σ) for s/c transponder.
Station Locations	Consider	10 cm	–	DSN level errors - including all tidal loads, drifts, and GPS based surveys

The utility of the landmark tracking data for absolute (inertial) navigation as well as target relative navigation is predicated on the quality/precision of a database of celestial objects and surface landmarks that have been ascertained from a precision DEM. For future lunar landings at the Moon the DEM will be derived from the detailed topography mapping campaign of LRO. It has been requested by the Exploration program that NASA's Lunar Mapping and Modeling Project (LMMP) produce a global lunar DEM using the LRO data with a 25 m resolution and for regions within 5 km radius around designated landing sites a resolution of 2.5 m. This resolution has been assumed for the results of this research. Additionally, this information will be used to assess not only inertial navigation performance, but landing site relative navigation performance

Table 3: Optical Navigation Error Processes and Modeling

Error Source	Filter Parameter Type	A Priori Uncertainty (1σ)	Correlation Time/Distance	Update Time	Reasoning/ Comments
Camera Measurement Noise	-	0.1 pixel in sample and line	-	Per optical measurement	Uncertainty in the sample and line coordinates recorded by the camera
DEM Resolution Errors	-	25 m Globally, 2.5 m when 5 km from landing	-	Per optical measurement	Treated as an additive white noise process on the measurement
Lunar Map Tie Error	1st-Order Gauss–Markov Stochastic	150 m Globally, 2.5 m when 5 km from Landing	5 km (global) 0 m (white noise near landing site)	5 sec	
Camera Pointing Errors	White Noise Stochastic	1.3 mrad	-	60 sec	Scan platform random pointing error

Table 5: Accelerometer Performance Specifications and Attitude

Error Source	Parameter Type	A Priori Uncertainty (1σ)	Correlation Time	Update Frequency
Scale Factor Errors	1st-Order Gauss–Markov	150 ppm	2 hrs	20 Hz
Bias Errors	1st-Order Gauss–Markov	30 μg	2 hrs	20 Hz
Orthogonality Errors	1st-Order Gauss–Markov	20 Arcsec	2 hrs	20 Hz
IMU Misalignment Errors	Estimate Random Bias	0.2 mrad	-	20 Hz
Velocity Random Walk	Random Walk	1.3e-5 m/s/sqrt(s)	-	20 Hz
Per-Axis Attitude Uncertainties	1st-Order Gauss Markov	0.57 mrads	10 secs	20 Hz

as well.

Inertial Measurement Unit: Finally, the navigation sensor system consisting of the radar altimeter/velocimeter, gimbaled op-nav camera system, and radiometric transponder is completed with an Inertial Measurement Unit (IMU) providing a direct measure of inertial accelerations and attitude rates. The accelerometers in the IMU, via an internal integration process, provide a measure of the accumulated non-gravitational delta-velocities (in the IMU case frame) on a 20 Hz rate during powered maneuvering phases. Detailed model information is provided by Ely (Reference [1]) and the performance characteristics of the accelerometers are listed in Table 5. One important point needs to be noted about how the accelerometer data is used in the current work; rather than with dead-reckoning, it is processed as a measurement in the filter. Doing this more fully integrates the diverse set of navigation data in the filter via ensuring the spectral content (from the measurement partials) of all the instruments is properly accounted. Finally, the rate gyros in the IMU provide a measure of the delta angle changes, also on a 20 Hz rate. These measurements along with a star tracker that is making attitude fixes every 10 seconds provides a measure of the lander attitude that is accurate to better than 0.57 mrads.[13] As noted previously, the simulation is 3-DOF, but the attitude error process is modeled as a white noise stochastic process (see Table 5) that de-weights the IMU, altimeter, velocimeter, and landmark tracking through these measurements' partials sensitivity to attitude errors (and pointing errors).

RESULTS

The following results will show current state uncertainties of the navigation filter in both inertial coordinates and landing site relative coordinates. The filter is designed to provide direct inertial estimates of the both the lander and the landing site. So in cases with only the IMU and the radar active the landing site estimates remain at a priori values because neither the IMU nor the radar data is directly sensitive to the landing site; however, landmark tracking with the gimbaled camera system is sensitive to the landing site when it is being imaged. So in cases with the camera active the landing site estimates will improve upon the a priori values and in cases without it the uncertainties stay fixed at a priori values. The relationship between inertial and landing site relative estimates can be formulated using only the filter's inertial estimates as follows. Define the landing site relative position vector $\Delta\mathbf{r}_L$ as

$$\Delta\mathbf{r}_L = \mathbf{T}_i^{lf}\mathbf{r} - \mathbf{R}_L = \begin{bmatrix}\mathbf{T}_i^{lf} & -\mathbf{1}\end{bmatrix}\begin{bmatrix}\mathbf{r}\\ \mathbf{R}_L\end{bmatrix} \tag{45}$$

where, as before, $\mathbf{r}$ is the inertial position vector of the lander, $\mathbf{T}_i^{lf}$ is the rotation from inertial coordinates to body fixed coordinates, $\mathbf{R}_L$ is the landing site position vector in the body fixed frame, and $\begin{bmatrix}\mathbf{r} & \mathbf{R}_L\end{bmatrix}^{\mathrm{T}}$ is a portion of the filter's state vector. Using the linear transformation property of covariance matrices

$$\mathbf{y} = \mathbf{A}\mathbf{x} \quad \rightarrow \quad \mathbf{P}_{yy} = \mathbf{A}\mathbf{P}_{xx}\mathbf{A}^{\mathrm{T}}, \tag{46}$$

leads to the following landing site relative covariance expression

$$\mathbf{P}_{\Delta r \Delta r} = \mathbf{T}_i^{lf}\mathbf{P}_{rr}\left(\mathbf{T}_i^{lf}\right)^{\mathrm{T}} + \mathbf{P}_{LL} - \mathbf{T}_i^{lf}\mathbf{P}_{rL} - \mathbf{P}_{Lr}\left(\mathbf{T}_i^{lf}\right)^{\mathrm{T}}, \tag{47}$$

where the filter covariance matrix is subdivided as follows

$$\begin{bmatrix}\mathbf{P}_{rr} & \mathbf{P}_{rL} \\ \mathbf{P}_{Lr} & \mathbf{P}_{LL}\end{bmatrix}. \tag{48}$$

Note that covariance $\mathbf{P}_{LL}$ is initialized a priori with any existing map-tie errors and DEM resolution errors.

South Pole Landing

Lunar Orbit Navigation with EBGS Radiometrics and the OpNav Landmark Tracking: Begin by examining the lunar orbit results for the South Pole landing case. The lunar orbit determination, shown in Figure 7, illustrates the 3-sigma position uncertainty (shown in the upper subplot) of the lander while in the 100 x 100 orbit for the case with EBGS radio tracking (view periods shown in the bottom subplot) and landmark tracking from both the gimbaled wide angle camera (WAC) and narrow angle camera (NAC). Three types of position uncertainty are shown – a blue line for the lander's uncertainty relative to the landing site, a red line for the lander's inertial uncertainty (which can't be seen because it lies underneath the blue line), and a green line for the landing site's surface fixed position uncertainty. Since the WAC and NAC are imaging the landing site the knowledge of its location is improving, this is one of the benefits of having an imaging campaign of the landing site prior to landing. The period of time that this plot covers is 24 hrs with PDI occurring at the right. The red dashed line just to the left of PDI corresponds to the de-orbit maneuver that transfers to the 100 x 15.24 orbit. It can be seen that the filter knowledge of the lander location at the start of powered descent is ~ 100 m (3-sigma). Note that at about 10 minutes prior to PDI is the last of the radiometric tracking and there is no accelerometer or velocimeter data. There is a small period of altimeter data beginning just before PDI. This case represents a nominal result with the full complement of navigation sensors.

Descent and Landing with IMU-Only: Begin the South Pole landing analysis by considering the case of landing with an IMU-only. These results are shown in Figure 7 beginning at the initiation of the powered descent (PDI) and ending at landing. As before, the top plot in the figure shows the current state 3-sigma position uncertainty as a function of time, and the lower plot identifies the time periods of the active navigation instruments. In this result only the accelerometers are active (The rate gryos and star trackers, used primarily for attitude estimation, are also active, but not shown). There is no landmark tracking from the gimbaled passive camera system nor is there any Earth-based radiometric tracking. At the start (PDI) the descent filter is initialized with a position knowledge of ~ 600 m (3-sigma) that represents the navigation state knowledge based on Earth based tracking *only* (no OpNav as in the prior result) until 10 minutes prior to PDI. As expected, the position knowledge degrades over time slowly to a maximum of ~ 1100 m (3-sigma) at landing because it is integrating noise and bias errors in an open loop with

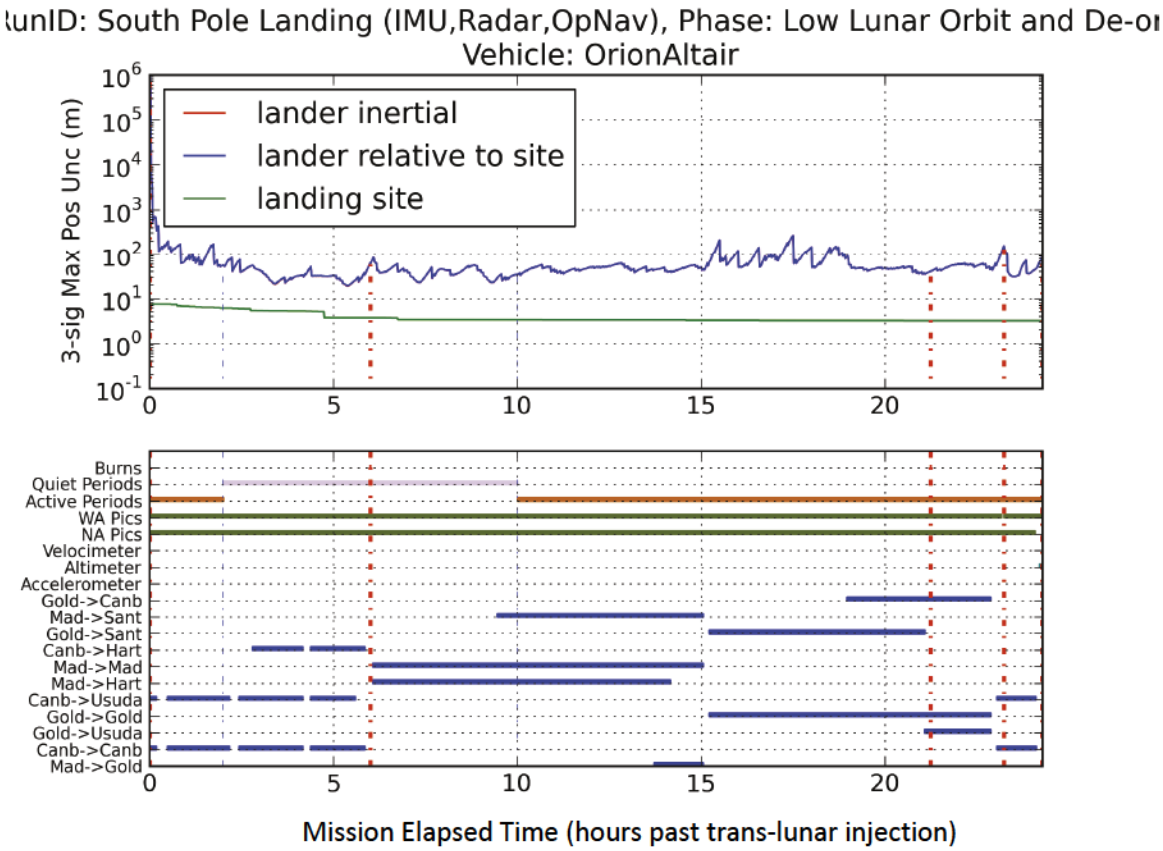

Figure 6: South Pole landing navigation 3-sigma position uncertainty while in lunar orbit with EBGS radiometric tracking and OpNav landmark tracking.

no external measurements to rectify the results. Also, the inertial and landing site relative uncertainties are, for all intents and purposes, the same.

Descent and Landing with IMU and Radar Altimetry and Velocimetry: This is the same case as before, but now the radar altimeter and velocimeter are active in addition to the IMU. The simulation results are presented in Figure 8. There is no landmark tracking from the camera system nor is there any Earth-based radiometric tracking. At the start (PDI) the descent filter is initialized with a position knowledge of ~ 200 m (3-sigma) that represents the navigation state knowledge based on Earth based tracking until 10 minutes prior to PDI plus a small amount of altimeter data (about 10 minutes worth). Compared to the prior results with the IMU-only, the addition of this small amount of altimeter data has improved the initial navigation filter knowledge by ~ 400 m (3-sigma). During most of the descent the accelerometer and the altimeter are active. The position knowledge degrades over time slowly to a maximum of ~ 400 m (3-sigma) when there is no velocimetry. Clearly, this is an improvement over the IMU-only case and illustrates the benefit of the altimetry even at high altitudes. In the last 180 seconds of the simulation, the velocimeter becomes active, and yields sufficient sensitivity to the inertial position to reduce the inertial uncertainty to ~ 2 m (3-sigma) by landing. The landing site relative uncertainties at landing are at the level of the DEM/map tie error associated with the landing site, ~ 9 m (3 sigma). This is a rather remarkable result, in that, with use of radar altimetry and velocimetry coupled with an accurate a priori map a precision landing has been obtained. Clearly, if the map tie is larger this will dominate the landing site relative solution, so, for instance, at Mars

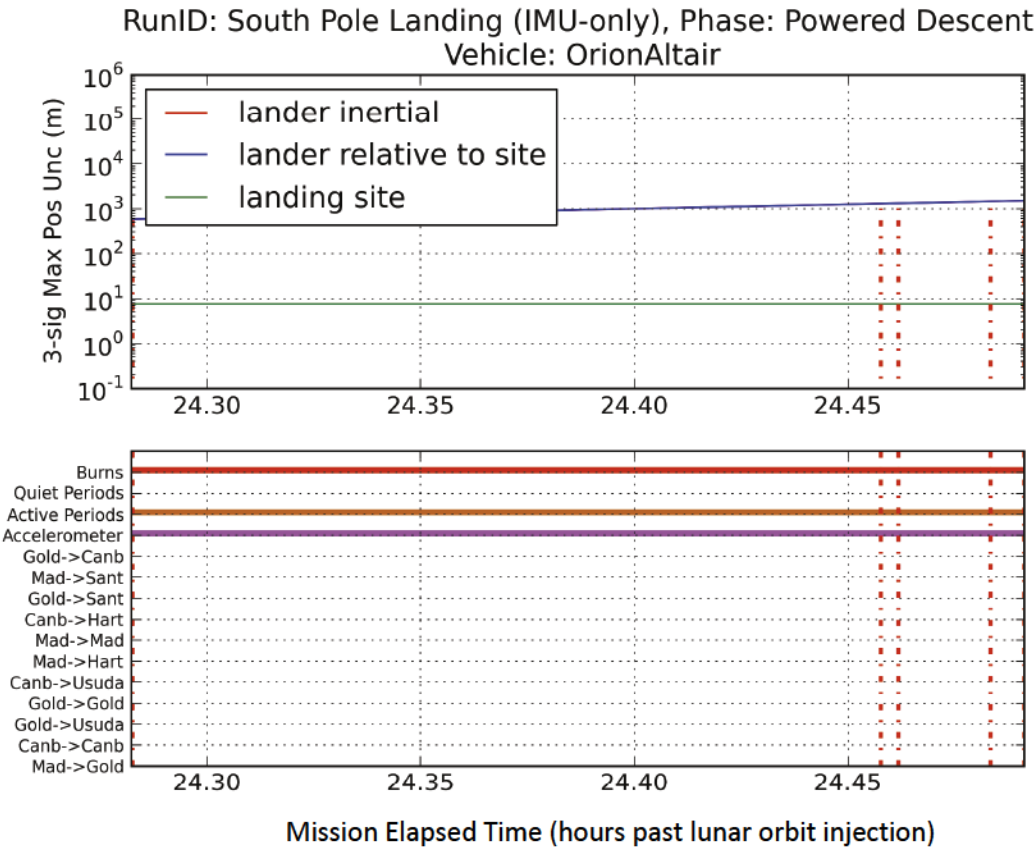

Figure 7: South Pole landing navigation 3-sigma position uncertainty during powered descent with only the IMU active.

where 400 m map tie errors are not uncommon; the inertial uncertainties will be insignificant relative to this error.

The terrain statistics for this case are shown in Figure 9 in two plots. The upper plot includes the altimeter measurement noise sigma (blue line) that clearly shows the noise dependence on altitude, the value of the lander uncertainty radius (green line) that is used to compute the terrain variability statistic, and then the computed terrain statistic (purple line) which is computed using

$$\sqrt{\sigma_{\max}^2\left[\left(\frac{\partial h}{\partial \Delta x'}\right)^2+\left(\frac{\partial h}{\partial \Delta y'}\right)^2\right]+\sigma_R^2}\ . \tag{49}$$

The lower plot shows the actual DEM heights (red line), which range between ± 5 km. It is noteworthy that the terrain statistic variations (purple line) are roughly correlated with the variations seen in the DEM (red line) and scale with the uncertainty radius (green line). Indeed, after the velocimeter comes on-line the uncertainty radius reduces dramatically as well as the associated terrain statistic. These behaviors suggest that the statistic calculation is properly deweighting the altimeter measurement.

Descent and Landing with IMU, Radar Altimetry and Velocimetry, and OpNav Landmark Tracking: The gimbaled OpNav camera is now added to the instrument suite. During powered descent the WAC is active, but the NAC is not because the distance is too close for its images to

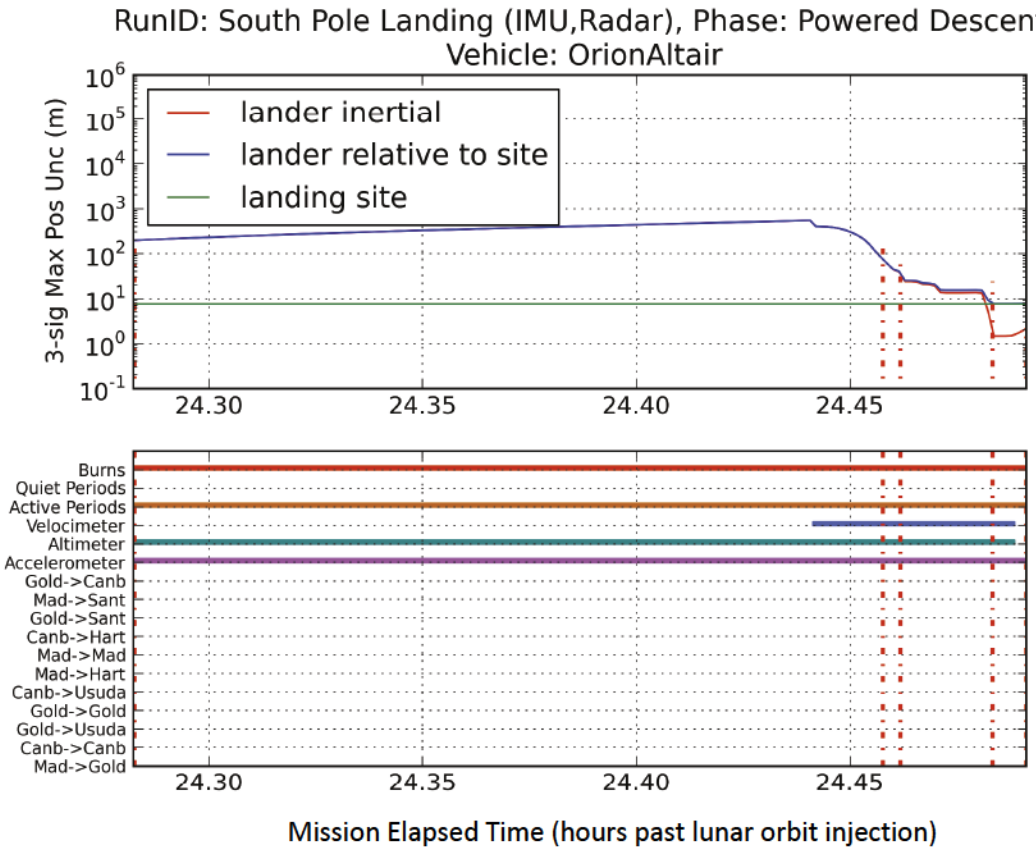

Figure 8: South Pole landing navigation 3-sigma position uncertainty during powered descent with the IMU and radar altimeter and velocimeter active.

be useful. The results for this case are exhibited in Figure 10. Since the camera system has been imaging while in lunar orbit the navigation filter at PDI has about a ~ 100 m (3 sigma) knowledge that is a better, by 100 m, than the prior case. Indeed, the uncertainties during the entire powered descent never increase significantly beyond 100 m and, by landing, improve to near ~ 2.4 m (3 sigma) in landing site relative coordinates. This precision landing result is expected since the landmark tracking is actively imaging the desired landing site, but, as just shown, this is also possible with only altimetry and velocimetry data.

Equatorial Landing

Descent and Landing with IMU-Only: Results for the equatorial lander are now explored. The lander's trajectory follows the equator fairly precisely so that the two cases, the South Pole landing following a meridian and this one, provide the boundaries of the radar altimeter and velocimeter performance as a function of orbital inclination. Ideally, an example in between would have been presented – this will be part of a future study. The equatorial landing using only the IMU during powered descent is shown in Figure 11. At PDI the uncertainty is ~ 240 m (3-sigma), which is better than the equivalent polar case at 600 m (3-sigma). However, there is nothing generic about this result other than a different epoch for the South Pole case would have yielded a different initial state at PDI for the navigation filter (for instance a few hours earlier the orbit uncertainty was under 100 m (3-sigma) in the South Pole case). At landing this case yields ~ 1000 m (3-sigma) landing uncertainty.

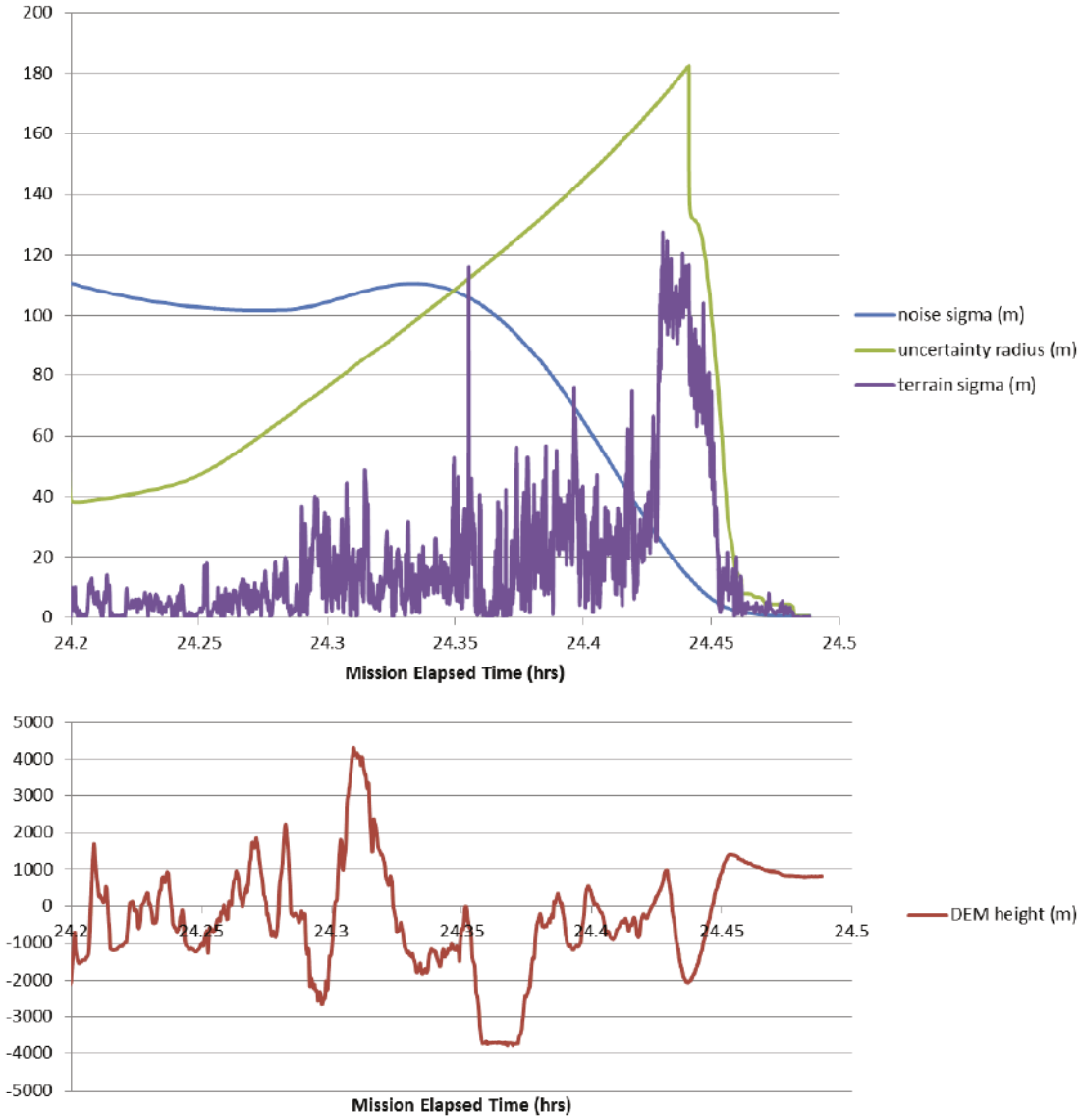

Figure 9: Terrain statistics for South Pole landing case.

Descent and Landing with IMU and Radar Altimetry and Velocimeter: The radar is now activated for this case with results given in shown in Figure 12. As before the altimeter does a good job of containing the growth of the IMU-based uncertainties. However, once the velocimeter becomes active the improvement in the uncertainties is not nearly as pronounced as it was in the South Pole case (see Figure 7); with the current case reaching a landing uncertainty of ~ 200 m (3–sigma). This can be explained via examination of the fundamental quantities in the velocimeter model, the inertial velocity $\mathbf{v}$ and the central body induced velocity $\boldsymbol{\omega}\times\mathbf{r}$. In the South Pole case these two vectors are nearly orthogonal to each other (albeit $\boldsymbol{\omega}\times\mathbf{r}$ is small in magnitude) so the both the velocity $\mathbf{v}$ and position $\mathbf{r}$ are observable and separable from each other. In the Equatorial case these two vectors are nearly anti-parallel to each other so $\mathbf{v}$ and $\mathbf{r}$ are not nearly as separable, thus leading to larger uncertainties for both. This observation also provides some insight as to what would happen with a landing at a mid-latitude. Under the hypothesis that the South Pole and Equatorial results are bounding cases, then a mid-latitude case would yield a land-

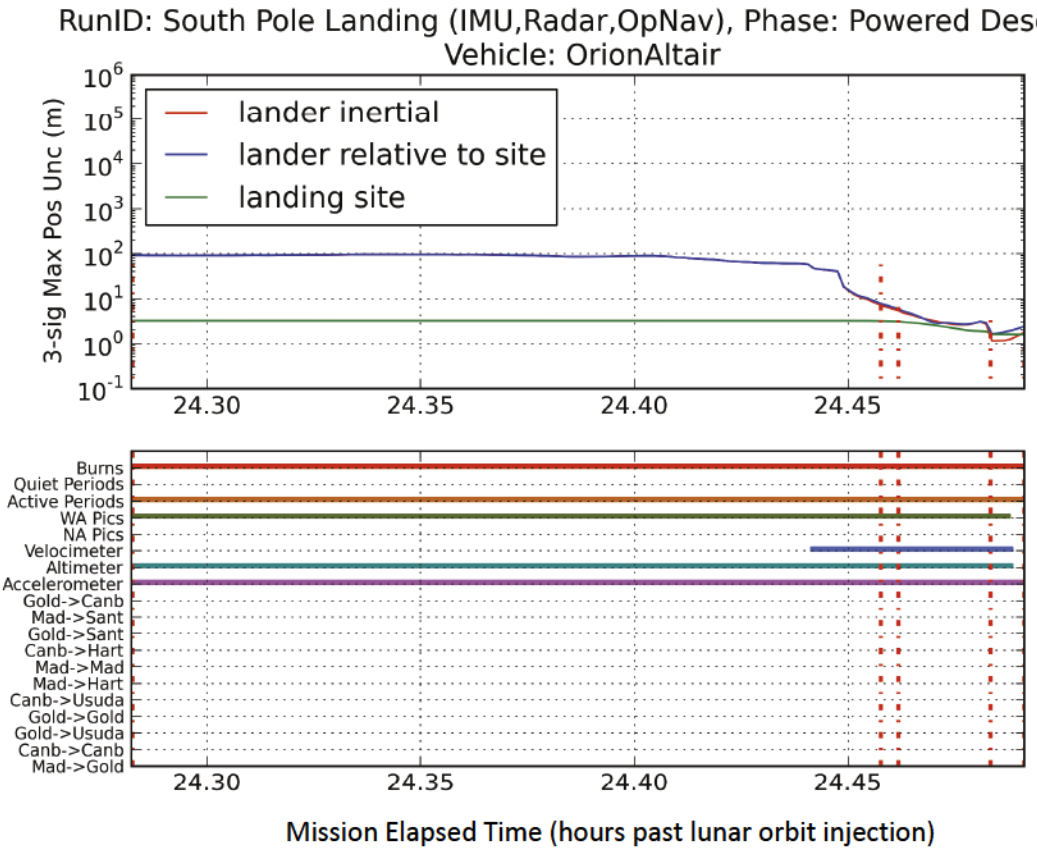

Figure 10: South Pole landing navigation 3-sigma position uncertainty during powered descent with the IMU, radar altimeter and velocimeter, and OpNav landmark tracking active.

ing uncertainty somewhere between 10 m and 200 m (3-sigma) and is dependent on the separation of the vectors $\mathbf{v}$ and $\boldsymbol{\omega}\times\mathbf{r}$.

Descent and Landing with IMU, Radar Altimetry and Velocimetry, and OpNav Landmark Tracking: In this final case the OpNav camera is active with the WAC taking pictures during powered descent. As with the South Pole case, the inclusion of active imaging of the landing site yields landing uncertainty relative to the site of approximately ~ 2 m (3-sigma).

CONCLUSION

The preceding results have shown that altimetry and velocimetry can be effectively used to improve inertial navigation of a lander by reducing landing uncertainties one to two orders of magnitude over an IMU-only landing navigation system. Indeed, in a South Pole landing case the velocimetry, coupled with an accurate a priori map, is sufficient for a precision landing navigation uncertainties at the ~ 10 m (3-sigma) level. To properly use the altimeter in an inertial estimator requires deweighting the data to account for terrain variations induced by differences in the lander navigation state and the lander's true state. Even with this deweighting, the altimetry data is capable of significantly reducing the open-loop error growth that is typical with IMU-only solutions. The addition of the velocimetry data can have a profound effect at reducing navigation uncertainties, but it is sensitive to the alignment of the $\mathbf{v}$ and $\boldsymbol{\omega}\times\mathbf{r}$ vectors. Indeed if these vectors are nearly orthogonal the velocimeter can be used to facilitate a precision landing, as the vec-

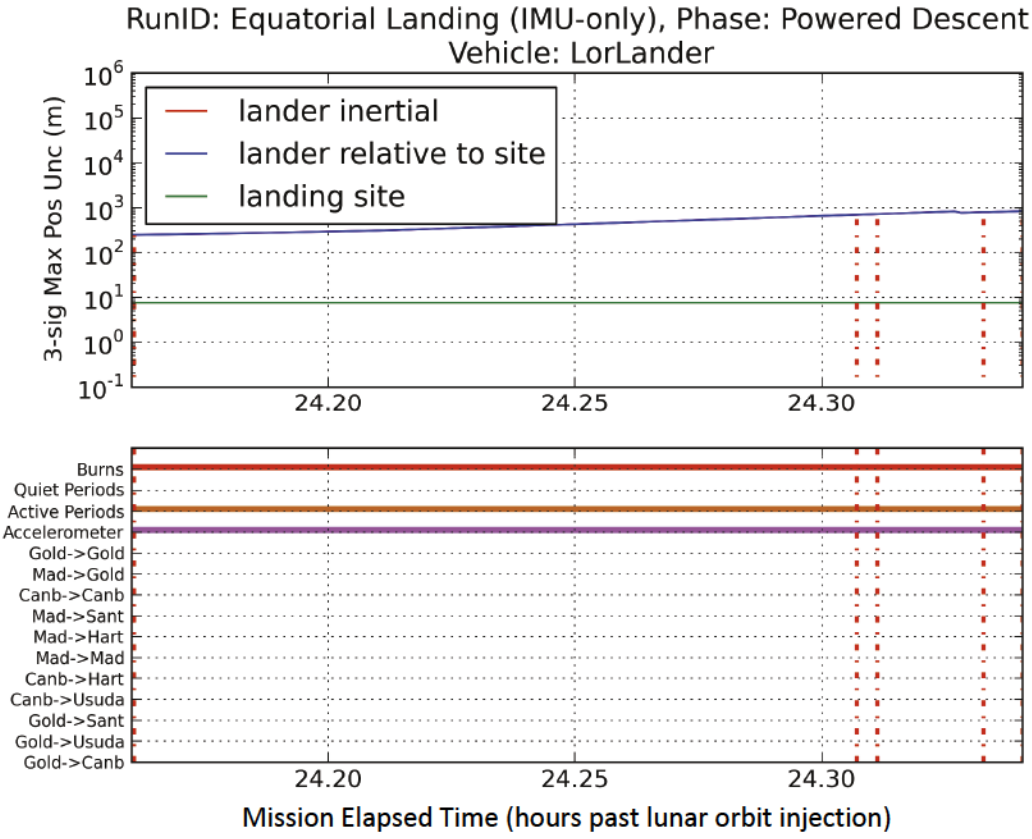

Figure 11: Equatorial Landing navigation 3-sigma position uncertainty during powered descent with only the IMU active.

tor separation decreases the benefit of the velocimeter data is reduced. Future work will focus on quantifying this effect via examining a larger set of trajectories as well as expanding the altimeter model to use the multi-beam slant range case.

ACKNOWLEDGMENTS

This work was carried out in part at the Jet Propulsion Laboratory, California Institute of Technology, under contract with the National Aeronautics and Space Administration.

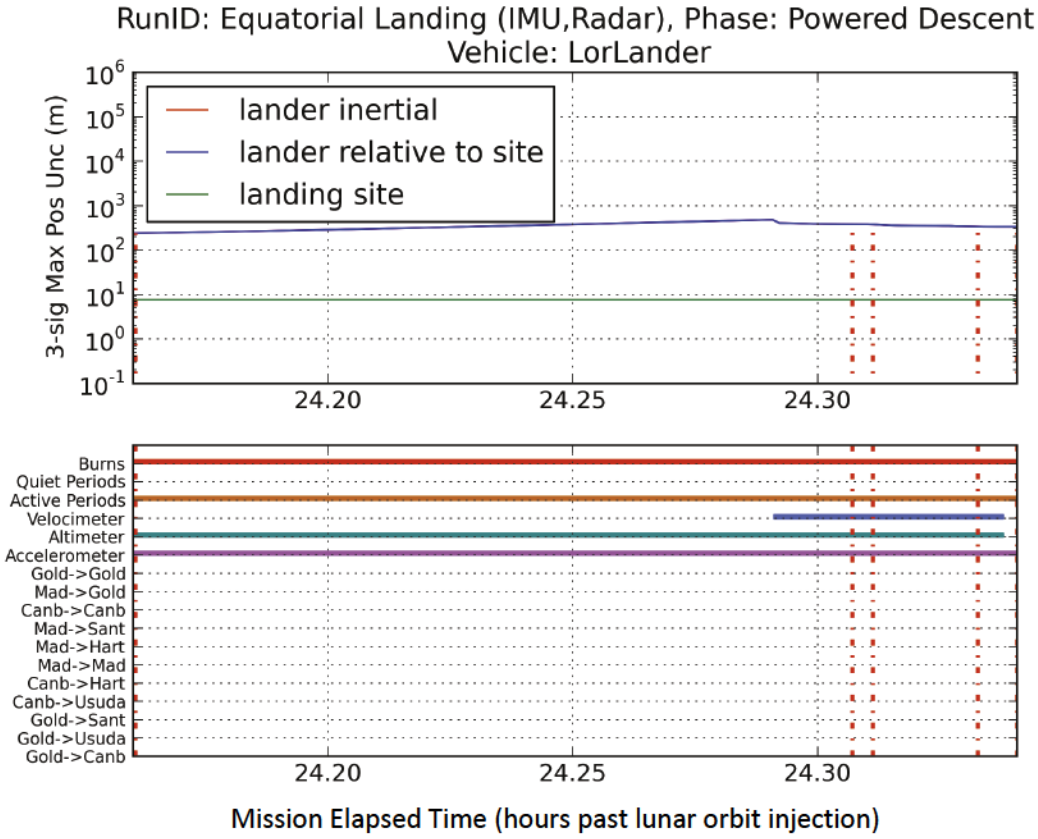

Figure 12: Equatorial Landing navigation 3-sigma position uncertainty during powered descent with only the IMU and radar altimeter and velocimeter active.

APPENDIX A: VEHICLE AND ENVIRONMENT FILTER ERROR MODELS

Table 6: Vehicle Non-Gravitational Errors (from uncoupled RCS and ECLSS) (a.k.a. FLAK) and Maneuver Execution Errors

Error Source	Parameter Type	A Priori Uncertainty (1σ)	Update Time	Reasoning/Comments	Reference
Active FLAK	Discrete White Noise	1.72467e-7 km/s^2 (~17.6 µg)	60 sec	Active during crew activity periods which are opposite of the intervals specified below	Levels are per Cx GNC and correlate into 0.5 km per 1/2 rev in lunar orbit. Cx guidelines on crew activity
Quiet FLAK	Discrete White Noise	1.72467e-8 km/s^2 (~1.76 µg)	60 sec	Quiet during crew sleep periods consistent with current Ops Concept WG assumptions (10/6/08)	Levels are per Cx GNC and correlate into 0.5 km per 1/2 rev in lunar orbit. Cx guidelines on crew activity

Aux Engine Maneuver Gates Execution Errors	Estimate Random Bias in each direction of impulse	10 mm/sec magnitude additive 0.1% magnitude scale factor 6 mm/sec direction additive 0.003 rad pointing	–	445 N Engine Burns	Altair LDAC 2 Burn execution analysis.
Main Engine Maneuver Gates Execution Errors	Estimate Random Bias in each direction of impulse	30 mm/sec magnitude additive 0.1% magnitude scale factor 10 mm/sec direction additive 0.003 rad pointing	–		Altair LDAC 2 Burn execution analysis.
EDS Engine Maneuver Gates Execution Errors	Estimate Random Bias in each direction of impulse	30 mm/sec magnitude additive 0.05% magnitude scale factor 10 mm/sec direction additive 0.003 rad pointing	–		Discussions with Altair integrated performance engineers

Table 7: Parameters of lunar Gravity First-Order Markov Models Due to Omitted Gravity Terms (above 100 x 100) in Descent Trajectory Propagation

Altitude	Vertical Component		Horizontal Component		
	$\sqrt{q}$ (mgals)	Correlation Distance (km)	$\sqrt{q}$ (mgals)	Correlation Distance Along (km)	Correlation Distance Across (km)
0 km	24.86	14.26	17.53	10.31	22.30
10 km	8.72	20.93	6.18	16.23	31.85
20 km	3.92	23.66	2.79	18.50	35.19
30 km	1.89	25.03	1.35	19.72	37.31
40 km	0.95	25.94	0.68	20.48	38.52
50 km and up	0.49	26.69	0.35	21.08	39.43

Table 8: Environmental Uncertainties

Error Source	Parameter Type	A Priori Uncertainty (1σ)	Correlation Time / Distance	Update Time	Reasoning/Comments
Earth Ephemeris	Considered	DE421 cov	–	–	Current lunar ephemeris knowledge.
Moon Ephemeris	Estimated Random Bias	DE421 cov	–	–	Current lunar ephemeris knowledge.

Earth Pole X, Y	1st-order Gauss–Markov stochastic	5 cm each component	48 hrs	6 hrs	
Earth UT1	1st-order Gauss–Markov stochastic	0.256 ms	48 hrs	6 hrs	Approximately 10 cm of orientation error
Earth Ionosphere–day/night	1st-order Gauss–Markov stochastic	55 cm/15 cm	6 hrs	1 hr	
Earth Troposphere–wet/dry	1st-order Gauss–Markov stochastic	1 cm/1 cm	6 hrs	1 hr	

REFERENCES

1. Ely, T.A., M. Heyne, and J.E. Riedel. *Altair Navigation during Trans-lunar Cruise, Lunar Orbit, Descent and Landing*. in *AIAA Guidance, Navigation, and Control Conference*. 2010. Toronto, Canada.
2. Lee, A.Y., et al., *An Overview of the Guidance, Navigation, and Control System Design of The Lunar Lander Altair*, in *AIAA Guidance, Navigation, and Control Conference*2010: Toronto, Canada.
3. Eichler, J., *A Performance Study of the Lunar Module's Landing Radar System.* J. Spacecraft, 1968. **5**(9): p. 6.
4. Euler, E.A., G.L. Adams, and F.W. Hopper, *Design and Reconstruction of the Viking Lander Descent Trajectories*. Journal of Guidance and Control, 1978. **1**(5).
5. Spencer, D.A., et al., *Mars Pathfinder Entry, Descent, and Landing Reconstruction.* Journal of Spacecraft and Rockets, 1999. **36**(3).
6. Desai, P.N.P., J. L., et al., *Entry, Descent, and Landing Performance of the Mars Phoenix Lander*, in *AIAA Guidance, Navigation, and Control Conferen*2008: Honolulu, Hawaii.
7. Shuang, L., et al., *MCAV/IMU integrated navigation for the powered descent phase of Mars EDL.* Advances in Space Research, 2010. **46**: p. 557 - 570.
8. Busnardo, D.M., et al., *LIDAR-Aided Inertial Navigation with Extended Kalman Filtering for Pinpoint Landing over Rough Terrain*, in *49th AIAA Aerospace Sciences Meeting*2011: Orlando, Florida.
9. Neumann, G.A. *Lunar Reconaissance Orbiter LOLA Instrument Science Data Archive*. 2011; Available from: http://imbrium.mit.edu/LOLA.html.
10. Pollard, B.D. and C.W. Chen. *The radar terminal descent sensor for the Mars Science Laboratory mission*. in *Aerospace Engineering Symposium*. 2009. Big Sky, MT.
11. Folkner, W., 2011.
12. Riedel, J.E., et al., *Optical Navigation Plan and Strategy for the Lunar Lander Altair*, in *AIAA Guidance, Navigation, and Control Conference*2010: Toronto, Canada.
13. Lee, A., *Updated Altair Attitude Estimation Perforamance*, 2010.